

Mechanism for Catalytic Stability Enhancement of FeIII[CoIII(CN)6] by Doping Divalent Ions for Organophosphate Hydrolysis

メタデータ	言語: English 出版者: ACS Publications 公開日: 2023-04-03 キーワード (Ja): プルシアンブルー類似体 キーワード (En): Prussian blue analogue, coordination polymer, replacement, durability, phosphoester 作成者: 関, 優介, 田部, 博康, 山田, 裕介 メールアドレス: 所属: Osaka City University, Kyoto University, Osaka City University
URL	https://ocu-omu.repo.nii.ac.jp/records/2020024

Mechanism for Catalytic Stability Enhancement of $\text{Fe}^{\text{III}}[\text{Co}^{\text{III}}(\text{CN})_6]$ by Doping Divalent Ions for Organophosphate Hydrolysis

Yusuke Seki, Hiroyasu Tabe, Yusuke Yamada

Citation	The Journal of Physical Chemistry C. 126, 12, 5564–5574
Issue Date	2022-03-31
Type	Journal Article
Textversion	Author
Supporting Information	The Supporting Information is available free of charge at https://doi.org/10.1021/acs.jpcc.2c00772 .
Rights	This document is the Accepted Manuscript version of a Published Work that appeared in final form in The Journal of Physical Chemistry C, copyright © 2022 American Chemical Society after peer review and technical editing by the publisher. To access the final edited and published work see https://doi.org/10.1021/acs.jpcc.2c00772 .
doi	10.1021/acs.jpcc.2c00772

Self-Archiving by Author(s)
Placed on: Osaka City University

Mechanism for Catalytic Stability Enhancement of $\text{Fe}^{\text{III}}[\text{Co}^{\text{III}}(\text{CN})_6]$ by Doping Divalent Ions for Organophosphate Hydrolysis

Yusuke Seki[†], Hiroyasu Tabe[§], and Yusuke Yamada^{*†‡}

[†]Department of Applied Chemistry and Bioengineering, Graduate School of Engineering,
Osaka City University, 3-3-138 Sugimoto, Sumiyoshi, Osaka 558-8585, Japan

[§]Institute for Integrated Cell-Material Sciences, Institute for Advanced Study, Kyoto
University, Yoshida-Hommachi, Sakyo, Kyoto 606-8501, Japan

[‡]Research Center for Artificial Photosynthesis (ReCAP), Osaka City University, 3-3-138
Sugimoto, Sumiyoshi, Osaka 558-8585, Japan

*E-mail: ymd@osaka-cu.ac.jp

KEYWORDS: Prussian blue analogue, coordination polymer, replacement, durability,
phosphoester

ABSTRACT: Catalytic activity and stability of iron hexacyanocobaltate ($\text{Fe}^{\text{III}}[\text{Co}^{\text{III}}(\text{CN})_6]$, **Fe-Co**) for organophosphate hydrolysis are improved by doping of divalent metal ions (**M** = Mn^{II} , Ni^{II} , or Cu^{II}). The catalytic activity of a series of ($\text{Fe}^{\text{III}}_{0.8}\text{M}^{\text{II}}_{0.3}$) $[\text{Co}^{\text{III}}(\text{CN})_6]$ (**FeM-Co**) was examined in a mixed solution of water and ethanol [9:1 (v/v)] containing disodium *p*-nitrophenyl phosphate (*p*-NPP) at 60 °C. **FeM-Co** compounds exhibited high conversions ($\geq 60\%$, 25 h), which are about four times that of **Fe-Co** (16%). Repetitive catalytic examinations indicated that the conversion at the 2nd runs in the systems using **FeM-Co** compounds maintained over 90% of those at the 1st runs. The low catalytic activity of **Fe-Co** in the mixed solution resulted from decomposition due to leaching of Fe^{III} ions by ligand exchange from CN ligand to *p*-NPP as evidenced by IR and XPS measurements for recovered precipitates after catalytic examination. Thus, the catalytic stability enhancement observed in **FeM-Co** compounds resulted from weaker interaction between *p*-NPP and Fe^{III} ions, which can be evidenced by reduced surface acidity evaluated from temperature programmed desorption of pyridine on the surfaces. The heats of pyridine adsorption (ΔH_s) on **FeM-Co** compounds surfaces were around 60-80 kJ mol^{-1} , which were less than half that of **Fe-Co** (160 kJ mol^{-1}). Based on these results, a mechanism is proposed for secure Fe-NC bonds and enhancement of the catalytic stability by doping of divalent metal ions to **Fe-Co**.

INTRODUCTION

Coordination polymers (CPs) and metal-organic frameworks (MOFs) have been regarded as promising materials to exhibit sophisticated catalysis contributing to mitigation of environmental issues. CPs and MOFs have designable and definite active sites of which coordination and electronic structures can be rationally optimized by appropriate choices of metal ions and bridging ligands.¹⁻¹⁷ CPs and MOFs have drawback on long term stability compared with conventional metal or metal oxide catalysts, resulting from high lability of metal-ligand bonds and reactivity of organic ligands under harsh reaction conditions.¹⁸⁻²⁰ The catalytic stability enhancement of CPs and MOFs has been a central issue, especially in aqueous media.

Cyano-bridged coordination polymers known as Prussian blue analogues are the simplest class of CPs, which can be easily obtained as precipitates by simply mixing aqueous solutions of an $[M^C(CN)_6]$ salt and an appropriate metal ion (M^N). Usually, water molecules coordinate to M^N ions to fulfill the octahedral coordination when a cyano-bridged coordination polymer contains more M^N ions than M^C ions. Thus, cyano-bridged coordination polymers can be used as heterogeneous catalysts for various reactions involving water as a substrate, such as hydrolysis of esters and photocatalytic water

oxidation, etc.²¹⁻³⁷ The activity of the coordination water molecules can be tuned by selecting an appropriate combination of M^C and M^N ions.³⁸

Organophosphate hydrolysis has been often chosen as a target reaction to evaluate the catalytic activity and stability of cyano-bridged coordination polymers.^{37,38} Organophosphates used as insecticides and herbicides are causative agents of poisoning accidents due to their strong toxicity.³⁹⁻⁴² Thus, the hydrolytic decomposition of organophosphate is necessary to reduce the strong toxicity.^{43,44} Such organophosphates hydrolysis has been efficiently catalyzed by a class of Zr^{IV} based MOFs such as UiO-66, NU-1000, and MOF-808 due to strong Lewis acidity of high valent Zr^{IV} ions.⁴⁵⁻⁴⁷ Also, the cyano-bridged coordination polymers composed of high valent metal ions, such as $Fe^{III}[Co^{III}(CN)_6]$ (**Fe-Co**), have been reported to exhibit high activity for the organophosphate hydrolysis.³⁸ However, the stability of some cyano-bridged coordination polymers during the catalytic reaction should be improved in neutral or alkaline solutions.

We report herein the enhanced catalytic activity and stability of **Fe-Co** by doping of divalent metal ions (M^{II}) to **Fe-Co** as N-bound metal ions. Manganese(II), nickel(II), and copper(II) ions are chosen as the M^{II} ions among 3d-metal ions, because (1) they are inactive for organophosphate hydrolysis, (2) the molar ratio of M^{II} ions to Fe^{III} and Co^{III}

ions can be quantitatively determined by elemental analyses, and (3) they have octahedral coordination structures in cyano-bridged coordination polymers as well as Fe^{III} ions. The catalytic stability and activity of cyano-bridged coordination polymers are evaluated for the hydrolysis of *p*-nitrophenyl phosphate (*p*-NPP). Then, the structures of coordination polymers after the catalytic reactions were analyzed by infrared (IR) spectroscopy and X-ray photoelectron spectroscopy (XPS) to discuss the contribution of doped M^{II} ions to the catalytic stability of coordination polymers. Additionally, the effect of M^{II} ions on the surface acidity of **Fe-Co** was also examined by temperature-programmed desorption of pyridine to discuss the deactivation mechanism of **Fe-Co**.

EXPERIMENTAL SECTION

Materials. Aqueous solutions were prepared with ultrapure water provided by a Barnstead Smart2Pure water purification system (Thermo Scientific, US) where the electronic conductance was 18.2 MΩ cm. All chemicals were used as supplied without further purification. Iron(III) nitrate nonahydrate, manganese(II) nitrate hexahydrate, nickel(II) nitrate hexahydrate, copper(II) nitrate trihydrate, disodium *p*-nitrophenyl phosphate hexahydrate, *p*-nitrophenol, sodium hydroxide, and pyridine were purchased from FUJIFILM-Wako Pure Chemical Industries Corporation. Potassium hexacyanocobaltate(III) was obtained from Strem Chemicals, Inc. 4-(2-Hydroxyethyl)-1-

piperazineethanesulfonic acid (HEPES) was obtained from Sigma-Aldrich Co. LLC. Carbonylchlorohydridotris(triphenylphosphine)ruthenium(II) was obtained from Tokyo Chemical Industry Co., Ltd.

Synthesis of $\text{Fe}^{\text{III}}[\text{Co}^{\text{III}}(\text{CN})_6]$ (Fe-Co). An aqueous solution of potassium hexacyanocobaltate (III) ($\text{K}_3[\text{Co}^{\text{III}}(\text{CN})_6]$, 0.10 M, 3.0 mL) was slowly added to an aqueous solution of iron (III) nitrate ($\text{Fe}^{\text{III}}(\text{NO}_3)_3$, 0.13 M, 3.0 mL) with vigorous stirring for 20 h at 40 °C. The formed precipitates were collected by centrifugation and washed with distilled water a couple of times. The precipitates were dried *in vacuo* for 12 h.

Synthesis of $(\text{Fe}^{\text{III}}_{0.8}\text{M}^{\text{II}}_{0.3})[\text{Co}^{\text{III}}(\text{CN})_6]$ (M = Mn, Ni, or Cu). An aqueous solution of $\text{K}_3[\text{Co}^{\text{III}}(\text{CN})_6]$ (0.10 M, 3.0 mL) was slowly added to an aqueous solution (3.0 mL) of $\text{Fe}^{\text{III}}(\text{NO}_3)_3$ (0.086 M) and divalent metal nitrate ($\text{M}^{\text{II}}(\text{NO}_3)_2$, 0.021 M) with vigorous stirring for 20 h at 40 °C. The formed precipitates were collected by centrifugation and washed with distilled water a couple of times. The precipitates were dried *in vacuo* for 12 h.

Synthesis of $(\text{Fe}^{\text{III}}_{0.4}\text{Mn}^{\text{II}}_{0.9})[\text{Co}^{\text{III}}(\text{CN})_6]$. An aqueous solution of $\text{K}_3[\text{Co}^{\text{III}}(\text{CN})_6]$ (0.10 M, 1.5 mL) was slowly added to an aqueous solution (1.5 mL) of $\text{Fe}^{\text{III}}(\text{NO}_3)_3$ (0.05 M) and divalent metal nitrate ($\text{Mn}^{\text{II}}(\text{NO}_3)_2$, 0.075 M) with vigorous stirring for 20 h at 40 °C. The

formed precipitates were collected by centrifugation and washed with distilled water a couple of times. The precipitates were dried *in vacuo* for 12 h.

Synthesis of $M^{II}_{1.5}[Co^{III}(CN)_6]$ (M-Co; M = Mn, Ni, or Cu). An aqueous solution of $K_3[Co^{III}(CN)_6]$ (0.10 M, 1.5 mL) was slowly added to an aqueous solution of divalent metal nitrate ($M^{II}(NO_3)_2$, 0.20 M, 1.5 mL) with vigorous stirring for 20 h. The formed precipitates were collected by centrifugation and washed with distilled water a few times. The precipitates were dried *in vacuo* for 12 h.

Physical Measurements. Scanning electron microscope (SEM) images of cyano-bridged coordination polymers were obtained using a JEOL JSM-6500F operated at 15 kV. The atomic ratios of coordination polymers were determined by X-ray fluorescence measurements using a Malvern PANalytical Epsilon 1. Powder X-ray diffraction patterns were recorded on a Rigaku MiniFlex 600. Incident X-ray radiation was produced by a Cu X-ray tube operating at 40 kV and 15 mA with Cu $K\alpha$ radiation ($\lambda = 1.54 \text{ \AA}$). The scan rate was 5° min^{-1} from $2\theta = 10\text{--}70^\circ$. Ultraviolet–visible (UV–vis) absorption spectra were recorded on a JASCO V–770 spectrometer. Infrared (IR) spectra were obtained on a Jasco FT/IR–6700 spectrometer with an attenuated total reflectance unit using a diamond window. Quantitative analyses of CN ligands in cyano-bridged coordination polymers were performed using

carbonylchlorohydridotris(triphenylphosphine)ruthenium(II) ($\text{Ru}^{\text{II}}(\text{CO})(\text{PPh}_3)\text{ClH}$) showing ν_{CO} at 1940 cm^{-1} as an internal standard with the content of 50 wt%. Nitrogen (N_2) adsorption-desorption isotherms at $-196\text{ }^\circ\text{C}$ were obtained with a MicrotracBEL Belsorp-mini II. Weighed samples ($\sim 50\text{ mg}$) were used for adsorption analysis after pretreatment at $150\text{ }^\circ\text{C}$ for 1 h *in vacuo*. The samples were exposed to N_2 within a relative pressure range from 0.01 to 101.3 kPa. The adsorbed amounts of N_2 were calculated from the pressure change in a cell after reaching equilibrium at $-196\text{ }^\circ\text{C}$. The total and external surface areas were calculated from the Brunauer–Emmett–Teller (BET) plot and *t*-plot, respectively. X-ray photoelectron spectroscopy (XPS) analyses were performed using a Shimadzu ESCA-3400HSE. An incident radiation was Mg-K α X-ray (1253.6 eV) at 200 W. The samples were mounted on a stage with double-sided carbon tape. The binding energy of each element was corrected by the C 1s peak (284.6 eV) from the carbon tape. Temperature-programmed desorption (TPD) measurements using pyridine were performed by a MicrotracBEL BELCAT II with vacuum pumps equipped with a glass tube with the inside diameter of 12 mm. Each cyano-bridged coordination polymer was first pretreated at $150\text{ }^\circ\text{C}$ for 1 h with a flow of helium (He , 50 mL min^{-1}), and then pyridine in an He flow (5 kPa , 50 mL min^{-1}) was adsorbed at $100\text{ }^\circ\text{C}$ for 30 min. After excess pyridine was removed with a flow of He at $150\text{ }^\circ\text{C}$ for 30 min, the temperature of

the bed was increased linearly at a rate of 2–10 °C min⁻¹ from 150 °C to 500 °C with a flow of He (30 mL min⁻¹). The desorbed pyridine was detected by a thermal conductivity detector (TCD) heated at 135 °C, and the intensity of the pyridine was calibrated with pyridine gas flow in a sample loop.

Catalysis Evaluation for Organophosphate Hydrolysis. A typical procedure for catalysis measurements is as follows: a mixed solution of water and ethanol [9:1 (v/v), 0.75 mL] containing disodium *p*-nitrophenyl phosphate (*p*-NPP, 10 mM) and a coordination polymer (3.0 mg, ~0.01 mmol of each monomer unit) in a sealed microtube was shaken at 900 rpm at 60 °C. An aliquot (10 µL) of the reaction mixture periodically sampled was diluted with a HEPES-NaOH buffer solution (2490 µL, 0.1 M, pH 8.3) for UV–vis spectra measurements. The conversion ratio of *p*-NPP at a certain reaction time was determined by the absorbance change at 400 nm ascribed to the formed *p*-nitrophenolate ion (*p*-NP, $\epsilon = 1.57 \times 10^4 \text{ M}^{-1} \text{ cm}$). Catalysts recovered by centrifugation were washed with distilled water after each run and used for further reactions under the same reaction conditions.

RESULTS AND DISCUSSION

Structures of $(\text{Fe}^{\text{III}}_{0.8}\text{M}^{\text{II}}_{0.3})[\text{Co}^{\text{III}}(\text{CN})_6]$ (FeM-Co**; **M = Cu, Mn, or Ni**) and $\text{Fe}^{\text{III}}[\text{Co}^{\text{III}}(\text{CN})_6]$ (**Fe-Co**).** A series of cyano-bridged coordination polymers, $(\text{Fe}^{\text{III}}_{0.8}\text{M}^{\text{II}}_{0.3})[\text{Co}^{\text{III}}(\text{CN})_6]$ (**FeM-Co**, **M = Cu, Mn, or Ni**) and $\text{Fe}^{\text{III}}[\text{Co}^{\text{III}}(\text{CN})_6]$ (**Fe-Co**) were prepared by mixing an aqueous solution containing metal salts and an aqueous solution of $\text{K}_3[\text{Co}^{\text{III}}(\text{CN})_6]$ to yield precipitates. The scanning electron microscope (SEM) images showed that the particles size of each coordination polymer was 0.5- 2 μm (Figure S1a-d). The contents of metal ions in the obtained precipitates were determined by X-ray fluorescence spectroscopy, suggesting that the molar ratio of metal ions of each coordination polymer was virtually the same as that predicted from the valence of metal ions and CN^- ions within an experimental error (Table 1). No contaminant potassium (K^+) ion was detected for **FeM-Co** compounds and **Fe-Co**.

Table 1. Expected and observed molar ratios of N-bound divalent metal ions (M^{II}), iron (Fe), and cobalt (Co) in a series of cyano-bridged coordination polymers determined by X-ray fluorescence measurements.

Coordination Polymer	M^{II}	Expected Molar Ratio		Observed Molar Ratio	
		$\text{M}^{\text{II}}/\text{Co}$	Fe/Co	$\text{M}^{\text{II}}/\text{Co}$	Fe/Co
$(\text{Fe}^{\text{III}}_{0.8}\text{Mn}^{\text{II}}_{0.3})[\text{Co}^{\text{III}}(\text{CN})_6]$ (FeMn-Co)	Mn^{II}	0.3	0.8	0.3	0.8
$(\text{Fe}^{\text{III}}_{0.8}\text{Ni}^{\text{II}}_{0.3})[\text{Co}^{\text{III}}(\text{CN})_6]$ (FeNi-Co)	Ni^{II}	0.3	0.8	0.33	1.0
$(\text{Fe}^{\text{III}}_{0.8}\text{Cu}^{\text{II}}_{0.3})[\text{Co}^{\text{III}}(\text{CN})_6]$ (FeCu-Co)	Cu^{II}	0.3	0.8	0.3	0.8
$\text{Fe}^{\text{III}}[\text{Co}^{\text{III}}(\text{CN})_6]$ (Fe-Co)	-	-	1.0	-	1.1

Powder X-ray diffraction (PXRD) patterns for **FeM-Co** compounds and **Fe-Co** were well agreed to those expected for the cubic structure (Figures 1a-d). The crystals of

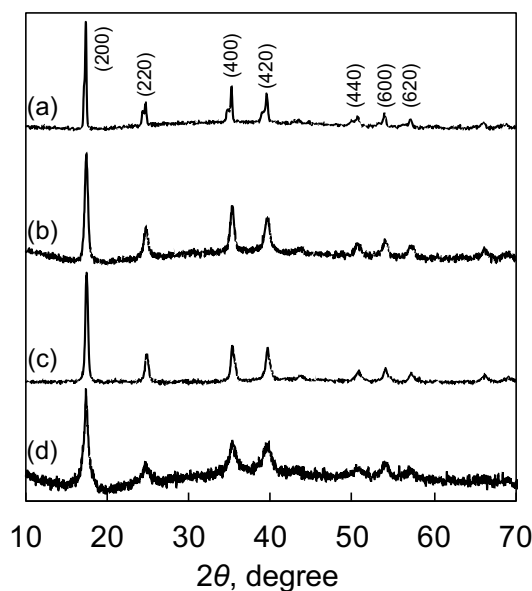


Figure 1. Powder X-ray diffraction (PXRD) patterns with Miller indices (hkl) of (a) $(\text{Fe}^{\text{III}}_{0.8}\text{Mn}^{\text{II}}_{0.3})[\text{Co}^{\text{III}}(\text{CN})_6]$ (**FeMn-Co**), (b) $(\text{Fe}^{\text{III}}_{0.8}\text{Ni}^{\text{II}}_{0.3})[\text{Co}^{\text{III}}(\text{CN})_6]$ (**FeNi-Co**), (c) $(\text{Fe}^{\text{III}}_{0.8}\text{Cu}^{\text{II}}_{0.3})[\text{Co}^{\text{III}}(\text{CN})_6]$ (**FeCu-Co**), and (d) $\text{Fe}^{\text{III}}[\text{Co}^{\text{III}}(\text{CN})_6]$ (**Fe-Co**).

FeNi-Co, **FeCu-Co**, and **Fe-Co** are single phase, however, two crystal phases were observed for **FeMn-Co**. The cell parameters (a) obtained for **FeNi-Co**, **FeCu-Co**, and **Fe-Co** were 10.19, 10.15, and 10.22 Å, respectively. The broad peaks of **Fe-Co** resulted from poor crystallinity or small-sized crystallites. **FeMn-Co** provided two cell parameters of 10.19 and 10.35 Å. The larger cell parameter similar to that (10.40 Å) of $\text{Mn}^{\text{II}}_{1.5}[\text{Co}^{\text{III}}(\text{CN})_6]$ (**Mn-Co**, Figure S2a) manifested that the Mn-rich phase contaminated

to Mn-poor phase. However, the Mn-rich phase showed no superior catalytic activity to Mn-poor phase, thus, the influence can be practically ignored (*vide infra*).

The CN stretching bands (ν_{CN}) of **FeMn-Co**, **FeNi-Co**, and **FeCu-Co** observed in infrared (IR) spectra appeared around 2179 cm^{-1} which is the same ν_{CN} value reported for **Fe-Co** (Figures 2a-d).^{35,48} These ν_{CN} peaks shifted to high wavenumbers compared

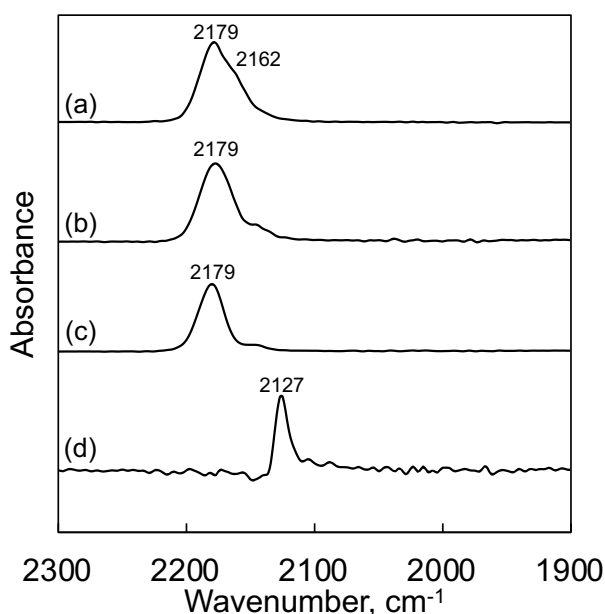


Figure 2. IR spectra of (a) $(\text{Fe}^{\text{III}}_{0.8}\text{Mn}^{\text{II}}_{0.3})[\text{Co}^{\text{III}}(\text{CN})_6]$ (**FeMn-Co**), (b) $(\text{Fe}^{\text{III}}_{0.8}\text{Ni}^{\text{II}}_{0.3})[\text{Co}^{\text{III}}(\text{CN})_6]$ (**FeNi-Co**), (c) $(\text{Fe}^{\text{III}}_{0.8}\text{Cu}^{\text{II}}_{0.3})[\text{Co}^{\text{III}}(\text{CN})_6]$ (**FeCu-Co**), and (d) $\text{K}_3[\text{Co}^{\text{III}}(\text{CN})_6]$.

with that of $\text{K}_3[\text{Co}^{\text{III}}(\text{CN})_6]$ (2127 cm^{-1}), because coordination of CN^- to a metal ion at the N side reduces the electron density of the antibonding orbitals of the CN bond.⁴⁹ **FeM-Co** compounds contain both $\text{Co}^{\text{III}}\text{-CN-Fe}^{\text{III}}$ and $\text{Co}^{\text{III}}\text{-CN-M}^{\text{II}}$ bonds, however, only one ν_{CN} peak was clearly observed for **FeNi-Co** and **FeCu-Co** as well as **Fe-Co**. On the other

hand, an obvious shoulder peak was observed for **FeMn-Co** around 2162 cm^{-1} assignable to the $\text{Co}^{\text{III}}\text{-CN-Mn}^{\text{II}}$ bond of Mn-rich phase. The position of the shoulder peak is close to ν_{CN} of **Mn-Co**, of which the presence was confirmed by XRD measurements (Figure S3a). The adsorption bands of metal-to-metal charge transfer (MMCT) for **FeM-Co** compounds were observed by UV-vis-near IR reflectance spectroscopy (Figures S4a-c). The absorption bands assignable to MMCT in near-infrared region were quite similar for **Fe-Co**, **FeNi-Co**, **FeCu-Co**, and **FeMn-Co**, indicating that the direct metal-metal interaction is limited between doped M^{II} and Co^{III} ions.

Nitrogen (N_2) adsorption-desorption isotherms of **FeM-Co** compounds and **Fe-Co** were obtained at $-196\text{ }^\circ\text{C}$ to clarify their porous structures. The total surface areas determined by the Brunauer-Emmett-Teller (BET) method calculated from the isotherms were 284 , 560 , 441 , and $135\text{ m}^2\text{ g}^{-1}$ for **FeMn-Co**, **FeNi-Co**, **FeCu-Co**, and **Fe-Co**, respectively (Figures S5a-d). The BET surface areas of **FeM-Co** compounds higher than that of **Fe-Co** seemed to be resulted from the number of defect sites predicted from $\text{M}^{\text{N}}/\text{M}^{\text{C}}$ ratios. **Fe-Co** with the $\text{M}^{\text{N}}/\text{M}^{\text{C}}$ ratio of 1 implies no defect sites formation, however **FeM-Co** compounds with $\text{M}^{\text{N}}/\text{M}^{\text{C}}$ ratio of 1.1 have some defect providing connected micropores.⁵⁰ Formation of micropores expected from the framework structures of **FeM-Co** compounds and **Fe-Co** was evidenced by the microporous (MP)

method. The window size of micropores of 0.6 nm was too small for *p*-nitrophenyl phosphate (*p*-NPP, ca. 1 nm) to penetrate into,³⁸ indicating that the inner surfaces are unavailable for the catalytic reaction. The inner and external surface areas of **FeM-Co** compounds and **Fe-Co** determined by the *t*-plot method were also tabulated in Table 2.

Table 2. Total surface areas determined by the Brunauer-Emmett-Teller (BET) method and external surface areas obtained by *t*-plot of $(\text{Fe}^{\text{III}}_{0.8}\text{M}^{\text{II}}_{0.3})[\text{Co}^{\text{III}}(\text{CN})_6]$ (**FeM-Co**; M = Mn, Ni, or Cu) and $\text{Fe}^{\text{III}}[\text{Co}^{\text{III}}(\text{CN})_6]$ (**Fe-Co**).

Coordination Polymer	BET Surface Area, m ² g ⁻¹	Inner Surface Area, m ² g ⁻¹	External Surface Area, m ² g ⁻¹	Pore Diameter, nm
FeMn-Co	284	271	13	0.6
FeNi-Co	560	210	350	0.6
FeCu-Co	441	168	273	0.6
Fe-Co	135	112	23	0.6

The external surface areas of **FeNi-Co** and **FeCu-Co** are much larger than those of **FeMn-Co** and **Fe-Co**. However, the inner and external surface areas insignificantly affected the heterogeneous catalysis as described below.

Heterogeneous Catalysis of FeM-Co Compounds and Fe-Co for the Hydrolysis of *p*-Nitrophenyl Phosphate. First, the hydrolysis of *p*-nitrophenyl phosphate (*p*-NPP) was examined in the reaction systems containing $\text{M}^{\text{II}}_{1.5}[\text{Co}^{\text{III}}(\text{CN})_6]$ without Fe^{III} ions (**M-Co**) to evaluate the direct contribution of M^{II} ions to the heterogeneous catalysis. The hydrolysis of *p*-NPP was examined at 60 °C in a mixed solution of water and ethanol [9:1

(v/v), 0.75 mL] containing a coordination polymer (3.0 mg, ~0.01 mmol of each monomer unit) and *p*-NPP (10 mM). The addition of 10% ethanol to the reaction solution effectively mitigated the decomposition of catalysts. The low conversions with **M-Co** compounds for 25 h, ca. 10%, indicated that the contribution of M^{II} ions to the catalysis of **FeM-Co** compounds was quite limited (Figure 3).

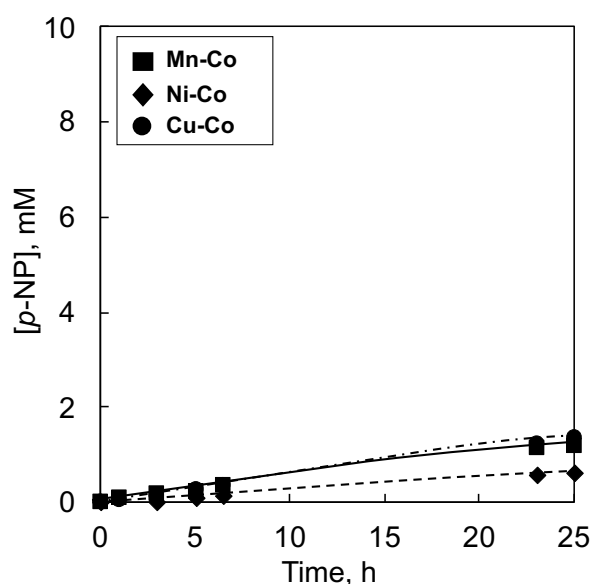


Figure 3. Time course of the formation of *p*-nitrophenol (*p*-NP) in a mixed solution of water and ethanol [9:1 (v/v), 0.75 mL] containing disodium *p*-nitrophenyl phosphate (*p*-NPP, 10 mM) and Mn^{II}_{1.5}[Co^{III}(CN)₆] (**Mn-Co**) (■), Ni^{II}_{1.5}[Co^{III}(CN)₆] (**Ni-Co**) (◆), or Cu^{II}_{1.5}[Co^{III}(CN)₆] (**Cu-Co**) (●) (3.0 mg).

Then, the catalytic activity of homogeneous Fe^{III} ions was examined in the reaction solution. Time-dependent UV-vis spectral changes were investigated for the reaction solutions containing Fe^{III} ions and **Fe-Co**. The absorption band assignable to

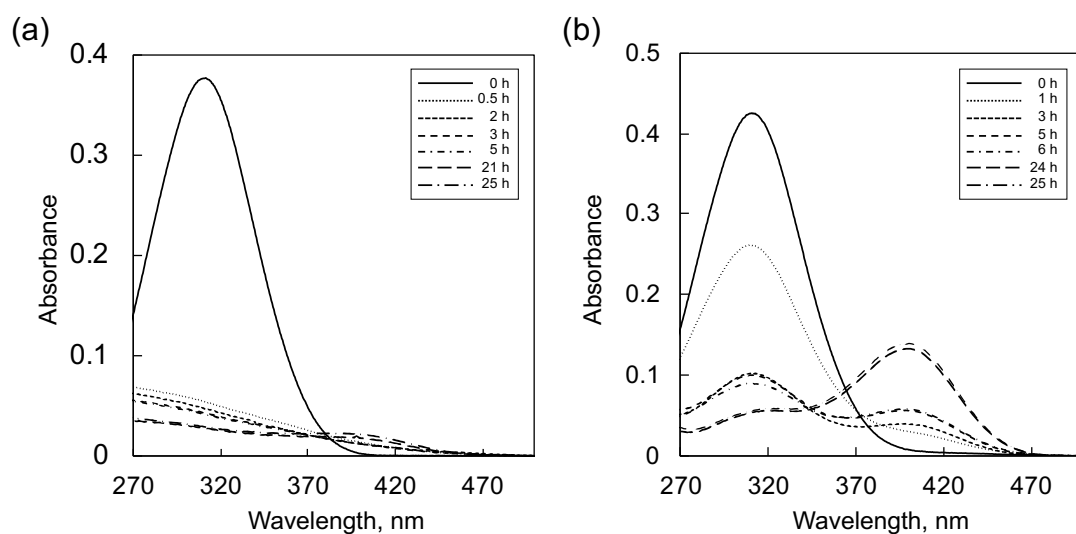


Figure 4. UV-vis absorption spectra of a mixed solution of water and ethanol (9:1 v/v, 0.75 mL) containing disodium *p*-nitrophenyl phosphate (*p*-NPP, 10 mM) and (a) Fe^{III}(NO₃)₃ (4.4 mg) or (b) Fe^{III}[Co^{III}(CN)₆] (**Fe-Co**) (3.0 mg). The spectra were obtained by adding an aliquot (10 μL) of the reaction solution in a HEPES-NaOH buffer solution (2490 μL, 0.1 M, pH 8.3). The absorption bands at 310 and 400 nm were assigned to *p*-NPP and *p*-nitrophenolate (*p*-NP) ions, respectively.

p-NPP around 310 nm almost disappeared without emerging the absorption band attributed to *p*-NP around 400 nm in the system using Fe^{III} ions (Figure 4a). These results indicated that the addition of *p*-NPP to the solution containing Fe^{III} ions forms precipitates. The UV-vis spectrum measurements for the solution containing **Fe-Co** indicated that the peak intensity of *p*-NPP suddenly decreased, however, the peak intensity of *p*-NP did not increase as expected from the decrease of *p*-NPP (Figure 4b). This result means that Fe^{III} ions in **Fe-Co** were partly coordinated by *p*-NPP to form precipitates as observed for the

solution containing $\text{Fe}^{\text{III}}(\text{NO}_3)_3$. The Fe^{III} ions remaining in the **Fe-Co** framework could contribute to the catalysis.

Catalytic activity of a series of cyano-bridged coordination polymers, **FeM-Co** compounds and **Fe-Co**, for the hydrolysis of *p*-NPP was examined at 60 °C in a mixed solution of water and ethanol [9:1 (v/v), 0.75 mL] containing a coordination polymer (3.0 mg, ~0.01 mmol of each monomer unit) and *p*-NPP (10 mM). The yield of the hydrolysis product, *p*-nitrophenolate ion (*p*-NP), was determined by characteristic absorbance change at 400 nm at a certain reaction time (Figure 5a). **Fe-Co** was reported to exhibit high activity for the hydrolysis of *p*-NPP in an aqueous solution, however its activity was low in a mixed solution.³⁸ On the other hand, **FeM-Co** compounds exhibited high activity with *p*-NPP conversions ($\geq 60\%$, 25 h) compared with those of **Fe-Co** (15%) and no catalyst (4%) (Figures 5b and S6a-d). The reaction was decelerated after 23 h, however, the catalytic activity was recovered at the 2nd run. The conversions at the 1st and 2nd runs with initial reaction rates (> 5 h) were summarized in Table 3. The conversions at the 2nd run for **FeMn-Co**, **FeNi-Co**, and **FeCu-Co** were 69 ± 3 , 55 ± 5 , and 60 ± 1 , respectively, which were virtually the same as those at 1st runs. The initial reaction rate at the 2nd run was similar to or slightly slower than those at the 1st run for each **FeM-Co** due to the partial loss of the catalysts during the recovering and washing processes.

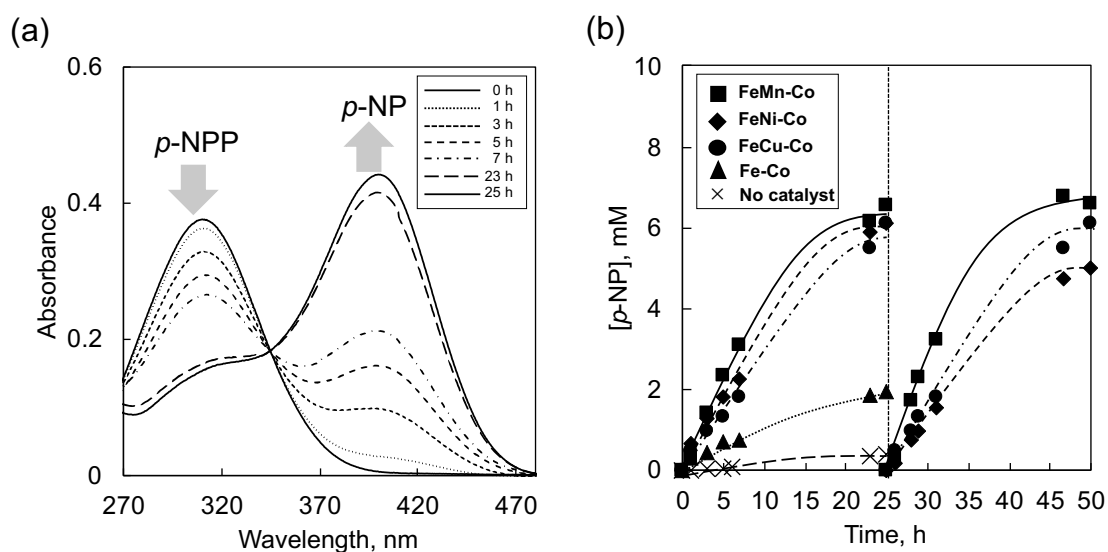


Figure 5. (a) UV-visible absorption spectra in a mixed solution of water and ethanol [9:1 (v/v), 0.75 mL] containing disodium *p*-nitrophenyl phosphate (*p*-NPP, 10 mM) and $(\text{Fe}^{\text{III}}_{0.8}\text{M}^{\text{II}}_{0.3})[\text{Co}^{\text{III}}(\text{CN})_6]$ (**FeM-Co**) (3.0 mg). The absorption maxima at 310 and 400 nm are assignable *p*-NPP and *p*-nitrophenolate ion (*p*-NP), respectively. (b) Time course of the formation of *p*-NP in the presence of $(\text{Fe}^{\text{III}}_{0.8}\text{Mn}^{\text{II}}_{0.3})[\text{Co}^{\text{III}}(\text{CN})_6]$ (**FeMn-Co**) (■), $(\text{Fe}^{\text{III}}_{0.8}\text{Ni}^{\text{II}}_{0.3})[\text{Co}^{\text{III}}(\text{CN})_6]$ (**FeNi-Co**) (◆), $(\text{Fe}^{\text{III}}_{0.8}\text{Cu}^{\text{II}}_{0.3})[\text{Co}^{\text{III}}(\text{CN})_6]$ (**FeCu-Co**) (●), $\text{Fe}^{\text{III}}[\text{Co}^{\text{III}}(\text{CN})_6]$ (**Fe-Co**) (▲), and no catalyst (×). The catalysts were centrifugally collected after the reactions for 25 h and used for the 2nd runs after washing.

Table 3. Comparison of catalytic activity of $(\text{Fe}^{\text{III}}_{0.8}\text{M}^{\text{II}}_{0.3})[\text{Co}^{\text{III}}(\text{CN})_6]$ (**FeM-Co** compounds; $\text{M}^{\text{II}} = \text{Mn}^{\text{II}}, \text{Ni}^{\text{II}}, \text{or Cu}^{\text{II}}$) and $\text{Fe}^{\text{III}}[\text{Co}^{\text{III}}(\text{CN})_6]$ (**Fe-Co**) for the hydrolysis of *p*-nitrophenyl phosphate (*p*-NPP, 10 mM) in a mixed solution of water and ethanol [9:1 (v/v), 0.75 mL] in the repetitive runs.

Coordination Polymer	1 st run		2 nd run	
	Conversion (%) ^a	Initial Rate, ^b $10^{-4} \text{ mol L}^{-1} \text{ h}^{-1}$	Conversion (%) ^a	Initial Rate, ^b $10^{-4} \text{ mol L}^{-1} \text{ h}^{-1}$
FeMn-Co	65 ± 1	5.7 ± 0.9	69 ± 3	5.9 ± 0.9
FeNi-Co	60 ± 1	5.0 ± 1.4	55 ± 5	2.8 ± 0.8
FeCu-Co	61 ± 0	3.8 ± 1.1	60 ± 1	3.3 ± 0.3
Fe-Co	16 ± 4	1.1 ± 0.3	–	–

^aConversions were calculated from the yields of *p*-nitrophenol (*p*-NP) at 25 h. ^bInitial rates were determined from the conversions for initial 1 h. The errors were calculated by at least two independent experiments under the same reaction conditions.

Similar catalytic activity was observed for **FeM-Co** compounds although **FeMn-Co** has much smaller external surface areas than **FeNi-Co** and **FeCu-Co** (Table 2). The high specific activity of **FeMn-Co** per surface area resulted from its high ability for *p*-NPP adsorption compared with those of **FeCu-Co** and **FeNi-Co**, because the rate determining step of the reaction has been reported as *p*-NPP adsorption on the catalyst surfaces. The *p*-NPP adsorption abilities of **FeM-Co** compounds were estimated from those of **M-Co** compounds ($M^{II}_{1.5}[Co^{III}(CN)_6]$; M = Mn, Ni, or Cu) where *p*-NPP hydrolysis could be practically ignored. The *p*-NPP adsorption abilities of **M-Co** compounds were examined in a mixed solution of water and ethanol [9:1 (v/v), 0.75 mL] containing *p*-NPP (10 mM) at 60 °C for 1 h (Figures S7a-c). The adsorbed amount of *p*-NPP on **Mn-Co** normalized by weight as 13.4 wt% was more than 10 times higher than those on **Ni-Co** and **Cu-Co** (1.2 and 1.3 wt%, respectively) although the BET surface areas of **Mn-Co**, **Ni-Co**, and **Cu-Co** were comparable as 874, 653, and 551 m² g⁻¹ (Figures S8a-c). Thus, high ability of *p*-NPP adsorption expected for **FeMn-Co** with relatively small external surface area resulted in catalytic activity comparable to **FeNi-Co** and **FeCu-Co** with much higher external surface area.

The effect of Mn-rich phase on the catalysis was scrutinized by the catalysis examination of $(Fe^{III}_{0.4}Mn^{II}_{0.9})[Co^{III}(CN)_6]$ (Figures S9a, b), which contained more Mn-

rich phase than **FeMn-Co**. The *p*-NPP conversion in a mixed solution of water and ethanol [9:1 (v/v), 0.75 mL] containing *p*-NPP (10 mM) and $(\text{Fe}^{\text{III}}_{0.4}\text{Mn}^{\text{II}}_{0.9})[\text{Co}^{\text{III}}(\text{CN})_6]$ (3.0 mg) for 25 h decreased to 54(\pm 3)% from 65(\pm 1)% observed for **FeMn-Co** under the same reaction conditions. Thus, Mn-poor phase seems to be suitable to obtain high catalytic activity. Catalytic stability of **FeMn-Co** was evaluated in repetitive experiments. The *p*-NPP conversion for the 2nd runs in the presence of **FeMn-Co** maintained over 90% of that for the 1st runs (Table 3). Thus, incorporation of Mn^{II} ions to **Fe-Co** framework effectively enhances the catalytic stability.

Catalytic performance of cyano-bridged coordination polymers in literature was summarized in Table S1 in terms of conversions for organophosphate hydrolysis in repetitive experiments. The repetitive catalysis measurements for the reaction system using $[\text{Cu}^{\text{II}}(\text{H}_2\text{O})_{8/3}]_{1.5}[\text{Fe}^{\text{II}}(\text{CN})_5(\text{NH}_3)]$ have been reported to exhibit decreased *p*-NPP conversion at the 2nd run, which was only 31% of that at the 1st run.³⁷ Moreover, *p*-NPP conversion at the 2nd run in the system using $[\text{Fe}^{\text{III}}(\text{H}_2\text{O})_{1.5}]_{4/3}[\text{Fe}^{\text{II}}(\text{CN})_6]$ was 71% of that at the 1st run.³⁸ On the other hand, *p*-NPP conversions at the 2nd runs in the reaction systems using **FeM-Co** compounds maintained over 90% of those at the 1st runs, indicating the enhancement of catalytic stability although the reaction conditions are not the same as those of previous studies.

The catalysis measurements of **FeM-Co** compounds were also performed in a 4-(2-hydroxyethyl)-1-piperazineethanesulfonate (HEPES) buffer solution (pH 8.0, 100 mM, 0.75 mL) without ethanol. Time courses of the *p*-NP formation and IR spectra of **FeM-Co** compounds and **Fe-Co** after the reactions were displayed in Figures S10 and S11a-d, respectively. The conversions for 25 h in the system using **FeMn-Co**, **FeNi-Co**, **FeCu-Co**, and **Fe-Co** were 61%, 50%, 75%, and 71%, respectively. However, the IR measurements indicated that the ν_{CN} peaks of **FeM-Co** compounds and **Fe-Co** almost disappeared, suggesting that **FeM-Co** compounds and **Fe-Co** decomposed during the catalytic reaction in an aqueous solution without ethanol.

Evaluation of Structural Stability by Quantitative IR Measurements. The structural stability of **FeM-Co** compounds and **Fe-Co** after the catalytic reactions was confirmed by quantitative IR spectroscopy. The IR measurements of **FeM-Co** in the presence of $\text{Ru}^{\text{II}}(\text{CO})(\text{PPh}_3)\text{ClH}$ ($\nu_{\text{CO}} = 1940 \text{ cm}^{-1}$) as an internal standard indicated that the intensity of ν_{CN} peaks observed for **FeM-Co** compounds after the reaction maintained more than 50% of those for pristine **FeM-Co** compounds (Figures 6a-c). On the other hand, the intensity of ν_{CN} peaks for **Fe-Co** decreased in ca. 90% after the reaction (Figure 6d), although insignificant intensity loss was observed when **Fe-Co** was immersed in a

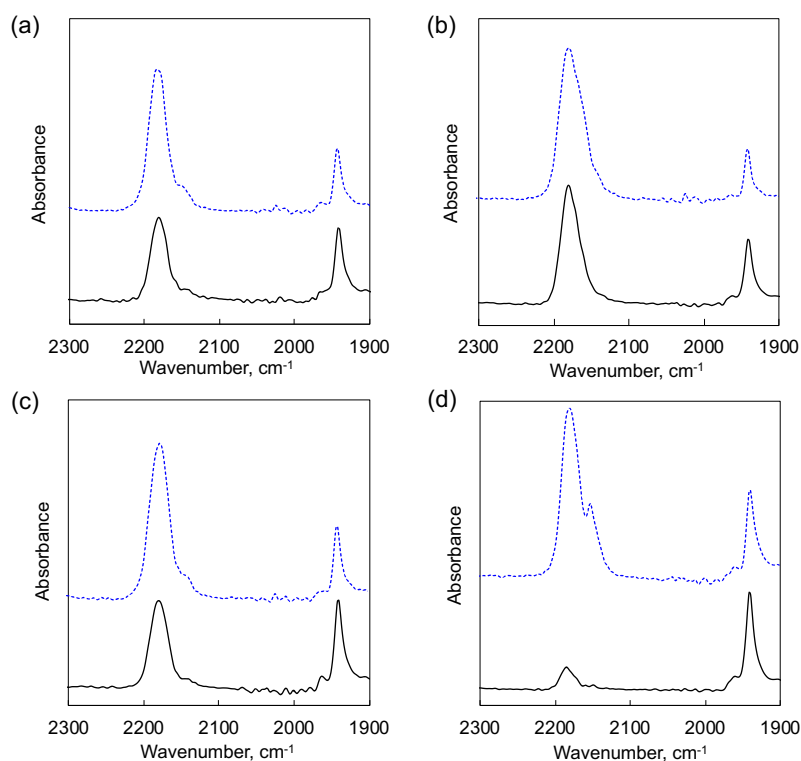


Figure 6. IR spectra (ν_{CN} and ν_{CO} regions) of (a) $(\text{Fe}^{\text{III}}_{0.8}\text{Mn}^{\text{II}}_{0.3})[\text{Co}^{\text{III}}(\text{CN})_6]$ (**FeMn-Co**), (b) $(\text{Fe}^{\text{III}}_{0.8}\text{Ni}^{\text{II}}_{0.3})[\text{Co}^{\text{III}}(\text{CN})_6]$ (**FeNi-Co**), (c) $(\text{Fe}^{\text{III}}_{0.8}\text{Cu}^{\text{II}}_{0.3})[\text{Co}^{\text{III}}(\text{CN})_6]$ (**FeCu-Co**), and (d) $\text{Fe}^{\text{III}}[\text{Co}^{\text{III}}(\text{CN})_6]$ (**Fe-Co**) before (blue dotted lines) and after (black solid lines) the catalytic reactions in the presence of internal standard (carbonylchlorohydridotris(triphenylphosphine)ruthenium(II) ($\text{Ru}^{\text{II}}(\text{CO})(\text{PPh}_3)\text{ClH}$), $\nu_{\text{CO}} = 1940 \text{ cm}^{-1}$). The catalysts were collected from the reaction solutions [water and ethanol: 9:1 (v/v), 0.75 mL] containing *p*-nitrophenyl phosphate (*p*-NPP, 10 mM). The fresh and recovered catalysts (0.60 mg) were mixed with $\text{Ru}^{\text{II}}(\text{CO})(\text{PPh}_3)\text{ClH}$ (0.60 mg) prior to the IR measurements.

reaction solution without *p*-NPP (Figure S12). These results clearly manifested that **Fe-Co** decomposed during the catalytic reaction. Thus, the doping of various divalent metal ions to **Fe-Co** enhances the structural stability during the reactions.

Identification of Adsorbed Species on FeM-Co and Fe-Co by IR and XPS. Repetitive reaction tests indicated that **FeM-Co** compounds maintain catalytic activity at the 2nd runs,

however, *p*-NPP conversions did not reach to 100% at the 1st runs even at elongated reaction time. A reason for the catalytic deterioration was investigated by IR and XPS measurements for the samples after catalytic reactions. IR spectra of the **FeM-Co** compounds after the reactions indicated the strong absorption bands around 1000 cm⁻¹ due to HPO₄²⁻ formed as a product of *p*-NPP hydrolysis as shown in Figures 7a-c. The

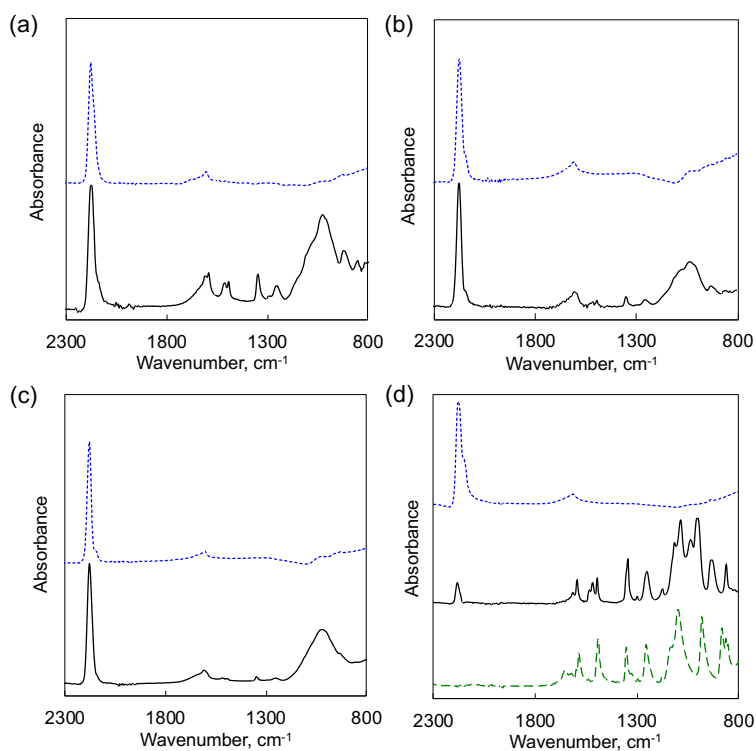


Figure 7. IR spectra of (a) (Fe^{III}_{0.8}Mn^{II}_{0.3})[Co^{III}(CN)₆] (**FeMn-Co**), (b) (Fe^{III}_{0.8}Ni^{II}_{0.3})[Co^{III}(CN)₆] (**FeNi-Co**), (c) (Fe^{III}_{0.8}Cu^{II}_{0.3})[Co^{III}(CN)₆] (**FeCu-Co**), and (d) Fe^{III}[Co^{III}(CN)₆] (**Fe-Co**) before (blue dotted lines) and after (black solid lines) the hydrolysis of *p*-nitrophenyl phosphate (*p*-NPP, 10 mM) in a mixed solution of water and ethanol [9:1 (v/v), 0.75 mL]. Green dashed line represents the spectrum of *p*-NPP in (d).

adsorption of HPO₄²⁻ on the surfaces of **FeM-Co** compounds would cause product inhibition. On the other hand, the IR spectra of **Fe-Co** after the catalytic reaction indicated

that *p*-NPP adsorbed on the surfaces (Figure 7d). The different adsorbed species could be also identified by X-ray photoelectron spectroscopy (XPS) measurements.

XPS measurements were performed to investigate the coordination environments and oxidation states of metal ions in **Fe-Co** and **FeM-Co** compounds before and after catalytic reactions. The XPS measurements of **Fe-Co** for the Co 2p region revealed that the Co ions maintained trivalent oxidation states during the reaction as evidenced by the lack of characteristic satellite peaks for divalent Co species (Figure 8a). However, the binding energies of Co 2p_{3/2} peak for **Fe-Co** after the 1st run (782.7 eV) increased compared with that for pristine **Fe-Co** (781.9 eV) by 0.8 eV. Also, the Fe 2p_{3/2} peak shifted from 711.3 to 712.7 eV after the reaction (Figure 8b). Addition to them, insignificant change in O 1s peaks originated from water molecules before and after the reaction suggested that water molecules constantly coordinated to the Fe ions during the reaction (Figure 8c). New peaks assignable to *p*-NPP appeared in P 2p and N 1s regions at 133.7, and 405.6 eV, respectively (Figures 8d, e). The higher energy shifts of the Co 2p and Fe 2p peaks after the reaction resulted from the partial liberation of CN ligands and alternative coordination of *p*-NPP during the reactions. The liberation of CN ligands and coordination of *p*-NPP in **Fe-Co** after the reaction were also evidenced by the IR measurements (Figure 7d). The weaker intensities of Co 2p peaks after the reaction imply

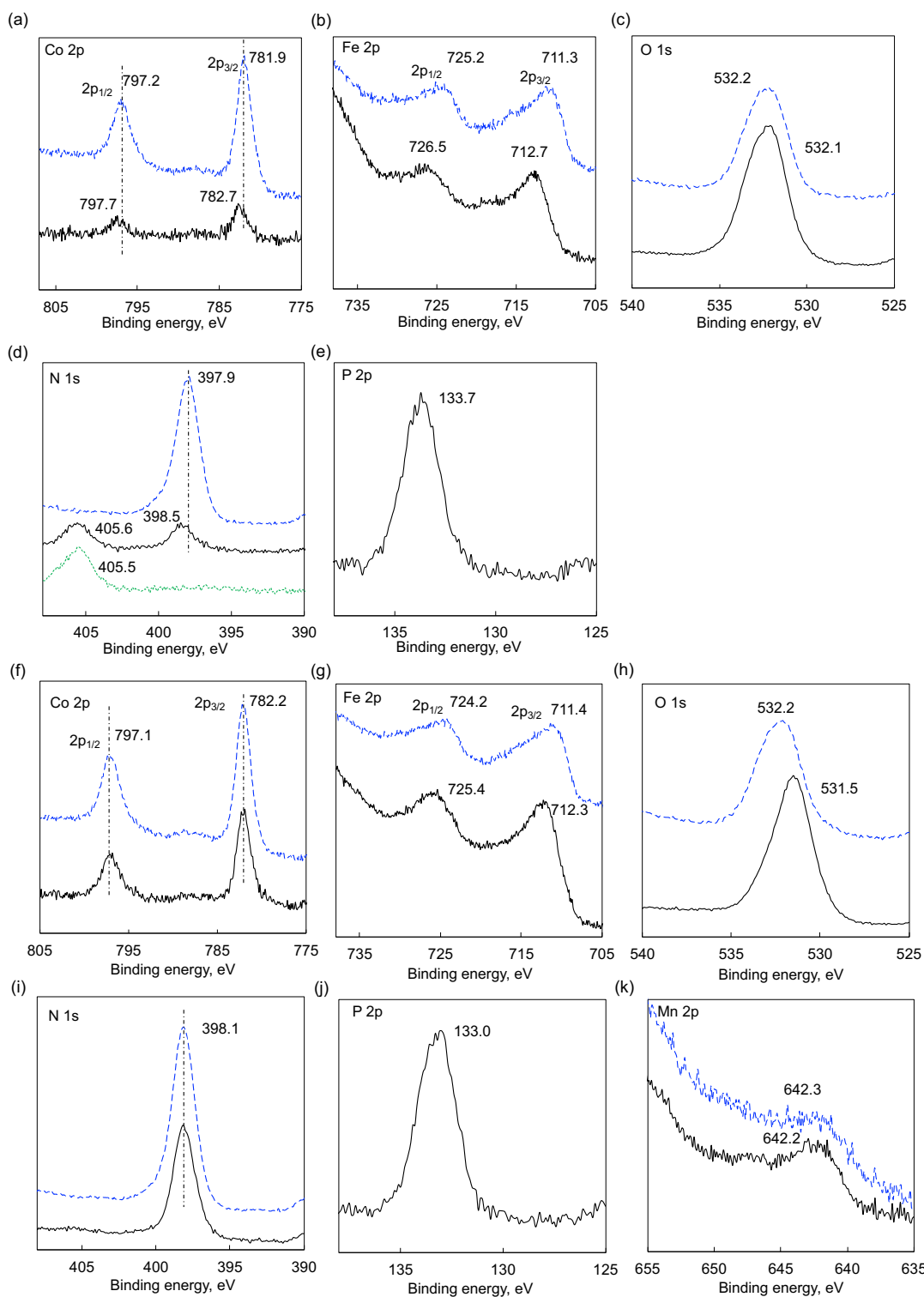


Figure 8. XPS spectra of (a-e) $\text{Fe}^{\text{III}}[\text{Co}^{\text{III}}(\text{CN})_6]$ (**Fe-Co**) and (f-k) $\text{Fe}^{\text{III}}_{0.8}\text{Mn}^{\text{II}}_{0.3}[\text{Co}^{\text{III}}(\text{CN})_6]$ (**FeMn-Co**) before (blue dotted lines) and after (black solid lines) the catalytic reactions. Green dotted line in (d) N 1s represents the spectrum of *p*-nitrophenyl phosphate (*p*-NPP).

the degradation of **Fe-Co** framework owing to the leaching of not only Fe ions but also Co species during the reaction.

XPS measurements for **FeMn-Co**, **FeNi-Co**, and **FeCu-Co** indicated that Co $2p_{3/2}$ peaks assignable to trivalent Co species observed at 782.0 ± 0.2 eV without satellite peaks as well as pristine **Fe-Co** (Figures 8f, S13a, g). The spin orbit splitting of Co $2p_{1/2}$ and Co $2p_{3/2}$ was 14.9 ± 0.2 eV. The peak positions and energy gaps were maintained for **FeMn-Co**, **FeNi-Co**, and **FeCu-Co** after the 1st runs, indicating insignificant change in both valence and coordination environment of Co ions during the reactions. On the other hand, broad Fe 2p peaks around 711.4 eV observed for pristine **FeMn-Co**, **FeNi-Co**, and **FeCu-Co** became sharper at 712.4 eV after the reactions, indicating that the coordination environment or the oxidation state of Fe ions has altered (Figures 8g, S13b, h). Also, the O 1s peaks appeared at 533.2 ± 0.2 eV due to coordinating water shifted to 531.6 ± 0.2 eV and P 2p peaks emerged, however, no new peaks appeared in the N 1s regions for **FeM-Co** compounds after the reactions (Figures 8h-j, S13c-e, i-k). These results clearly suggested that catalytically produced HPO_4^{2-} coordinated to Fe ions not *p*-NPP as suggested by IR measurements (Figures 7a-c). No obvious change was observed for the binding energies of Mn 2p, Ni 2p, and Cu 2p in **FeM-Co** compounds after the reactions although the peak intensity severely changed for **FeCu-Co** (Figures 8k, S13f, l). Thus,

XPS measurements also evidenced that the doping of divalent metal ions is effective to improve robustness of the **Fe-Co** framework.

Mechanism of High Catalytic Stability During the Hydrolysis of *p*-Nitrophenyl

Phosphate. The doping of divalent metal ions enhanced the catalytic stability of **Fe-Co**,

however, the mechanism is still unclear. The surface acidity of cyano-bridged coordination polymers has been reported to be deeply related with the catalytic behavior

in *p*-NPP hydrolysis, because the adsorption of *p*-NPP on the coordination polymers is

the rate-determining step.³⁸ The surface acidity of each **FeM-Co** was evaluated by the

temperature-programmed desorption (TPD) to determine the heat of desorption of

pyridine (ΔH).³⁸ The temperature of pyridine desorption-maximum (T_M) shifted by

changing the ramp rate (β) can be correlated with ΔH by using eq. 1 for all the

$$\ln \frac{T_M^2}{\beta} = \frac{\Delta H}{RT_M} + \ln \left[\frac{(1 - \theta)^2 V \Delta H}{FAR} \right] \quad (1)$$

coordination polymers, **FeM-Co** compounds and **Fe-Co**, in Figures S14a-c, where R , θ ,

V , F , and A stand for gas constant, surface coverage, catalyst volume, gas flow rate, and

frequency factor, respectively. ΔH s determined from the slopes for the plots of $\ln(T_M^2/\beta)$

vs $1/T_M$ were 80, 65, and 81 kJ mol⁻¹ for **FeMn-Co**, **FeNi-Co**, and **FeCu-Co**, respectively,

which were almost or less than half that of **Fe-Co**, 160 kJ mol⁻¹ (Figure 9).³⁸

The low surface acidity of **FeM-Co** compounds compared with that of **Fe-Co** suggested weaker interaction between *p*-NPP and Fe^{III} ions, preventing the decomposition

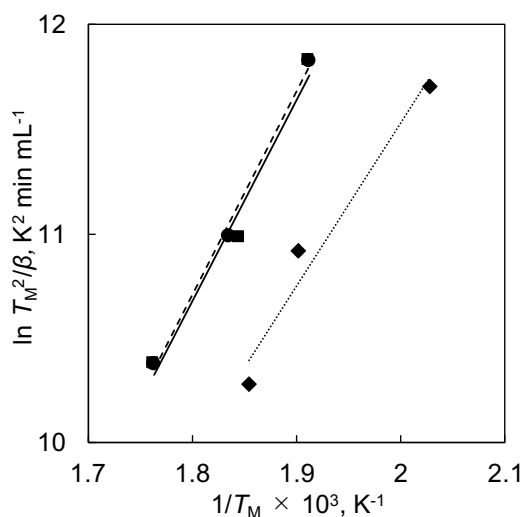
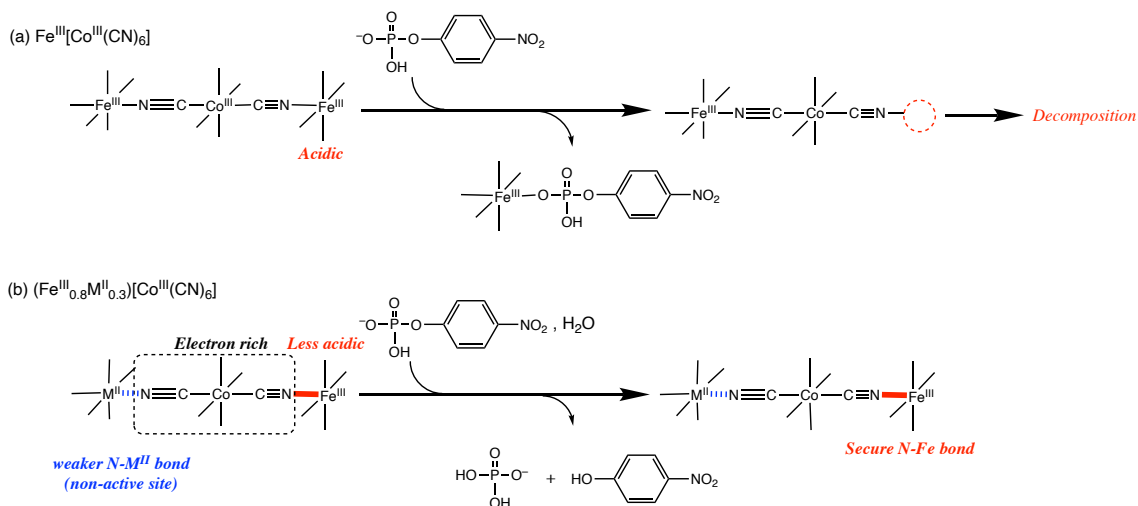


Figure 9. Plots of $\ln(T_M^2/\beta)$ vs $1/T_M$ of $(\text{Fe}^{\text{III}}_{0.8}\text{Mn}^{\text{II}}_{0.3})[\text{Co}^{\text{III}}(\text{CN})_6]$ (**FeMn-Co**) (■), $(\text{Fe}^{\text{III}}_{0.8}\text{Ni}^{\text{II}}_{0.3})[\text{Co}^{\text{III}}(\text{CN})_6]$ (**FeNi-Co**) (◆), and $(\text{Fe}^{\text{III}}_{0.8}\text{Cu}^{\text{II}}_{0.3})[\text{Co}^{\text{III}}(\text{CN})_6]$ (**FeCu-Co**) (●). T_M and β are the temperature of pyridine-desorption maximum and the ramp rate, respectively.

of the framework by leaching Fe^{III} ions (Scheme 1a). The mechanism is as follows: the doping of divalent M^{II} ions weakly interacting with CN ligand compared with the trivalent Fe^{III} ion results in providing a relatively electron rich state for $[\text{Co}^{\text{III}}(\text{CN})_6]^{3-}$ moiety (Scheme 1b). Then, the $[\text{Co}^{\text{III}}(\text{CN})_6]$ moiety more donating electron to an Fe^{III} ion at a surface results in low surface acidity and secure Fe^{III}-N bond to avoid leaching of Fe^{III} ions due to ligation of *p*-NPP. Thus, doping of divalent metal ions to **Fe-Co** enhances the catalytic stability for *p*-NPP hydrolysis.

Stability enhancement of cyano-bridged coordination polymers has been previously reported by doping divalent metal ions into the framework.⁵¹⁻⁵³ For example,



Scheme 1. Mechanism to enhance catalytic stability of $\text{Fe}^{\text{III}}[\text{Co}^{\text{III}}(\text{CN})_6]$ (**Fe-Co**) by doping divalent metal ions (M^{II}) for the hydrolysis of $p\text{-NPP}$ [(a) **Fe-Co** and (b) $(\text{Fe}^{\text{III}}_{0.8}\text{M}^{\text{II}}_{0.3})[\text{Co}^{\text{III}}(\text{CN})_6]$ (**FeM-Co**; $\text{M} = \text{Mn}, \text{Ni}, \text{or Cu}$)].

Cu^{II} doping enhanced the structural stability of the coordination polymers used as cathodes of sodium-ion batteries.⁵¹ Also, doping of Ni^{II} ions to Prussian blue to form $(\text{Fe}^{\text{II/III}}_x\text{Ni}^{\text{II}}_y)_z[\text{Fe}^{\text{II/III}}(\text{CN})_6]$ exhibited high stability for electrocatalytic H_2O_2 reduction in basic solutions compared with $\text{Fe}^{\text{II/III}}_x[\text{Fe}^{\text{II/III}}(\text{CN})_6]$.^{52,53} However, the mechanism for stability enhancement of the doped coordination polymers has yet to be fully elucidated. This is for the first time to propose the mechanism how to suppress the leaching of Fe^{III} ions from cyano-bridged coordination polymers by doping divalent metal ions based on IR and surface acidity measurements.

CONCLUSION

The catalytic activity and stability of $\text{Fe}^{\text{III}}[\text{Co}^{\text{III}}(\text{CN})_6]$ (**Fe-Co**) recognized as an effective catalyst for organophosphate hydrolysis were enhanced by doping divalent metal ions, which are inactive for the reaction as N-bound metal ions. The heterogeneous catalysis of the $(\text{Fe}^{\text{III}}_{0.8}\text{M}^{\text{II}}_{0.3})[\text{Co}^{\text{III}}(\text{CN})_6]$ (**FeM-Co**, M = Mn, Ni, or Cu) for the organophosphate hydrolysis examined in a solution containing *p*-nitrophenyl phosphate (*p*-NPP) clearly indicated that the doping of M^{II} ions into **Fe-Co** enhanced the catalytic stability by decreasing the degree of susceptibility to the Fe^{III} -N bond cleavage. So far, strong surface acidity has been believed to enhance the catalytic activity for organophosphate hydrolysis, however, we clearly demonstrate that strong surface acidity sometimes causes the leaching of Fe^{III} ions from the framework of a cyano-bridged coordination polymer. Therefore, optimum surface acidity is necessary to achieve both high catalytic activity and stability. This work provides new insights into design of CPs and MOFs with high stability in aqueous reaction solutions although further stability enhancement is necessary for practical applications.

ASSOCIATED CONTENT

Supporting Information. The Supporting Information is available free of charge on the ACS Publications website. Scanning electron microscope (SEM) images, powder X-ray diffraction (PXRD) patterns, nitrogen (N₂) adsorption-desorption isotherms, Ultraviolet–visible (UV–vis) spectra, Infrared (IR) spectra, X-ray photoelectron spectroscopy (XPS) spectra and temperature-programmed desorption (TPD) of pyridine spectra.

AUTHOR INFORMATION

Author Contributions

The manuscript was written through contributions of all authors. All authors have given approval to the final version of the manuscript.

Notes

The authors declare no competing financial interests.

ACKNOWLEDGMENT

This work was supported by Innovative Science and Technology Initiative for Security (ATLA, Japan) to Y. Y. (Nos. JPJ191047001), JSPS KAKENHI to Y. Y. (Nos. JP16H02268 and JP19KK0144) and to H. T. (Nos. JP20H05110 and JP21K14648), Grant for Research of the Japan Petroleum Institute, the Paloma Environmental Technology

Development Foundation, and the ENEOS Tonen General Sekiyu Research/Development

Encouragement and Scholarship Foundation to H. T.

REFERENCES

1. Wei, Y.-S.; Zhang, M.; Zou, R.; Xu, Q. Metal–Organic Framework-Based Catalysts with Single Metal Sites. *Chem. Rev.* **2020**, *120*, 12089-12174.
2. Dwyer, D. B.; Lee, D. T.; Boyer, S.; Bernier, W. E.; Parsons, G. N.; Jones, W. E. Toxic organophosphate hydrolysis using nanofiber-templated UiO-66-NH₂ metal-organic framework polycrystalline cylinders. *ACS Appl. Mater. Interfaces* **2018**, *10*, 25794-25803.
3. Xia, M.; Zhuo, C.; Ma, X.; Zhang, X.; Sun, H.; Zhai, Q.; Zhang, Y. Assembly of the active center of organophosphorus hydrolase in metal-organic frameworks *via* rational combination of functional ligands. *Chem. Commun.* **2017**, *53*, 11302–11305.
4. de Koning, M. C.; van Grol, M.; Breijaert, T. Degradation of paraoxon and the chemical warfare agents VX, tabun and soman by the metal-organic frameworks UiO-66-NH₂, MOF-808, NU-1000, and PCN-777. *Inorg. Chem.* **2017**, *56*, 11804–11809.

5. Lee, D. T.; Zhao, J.; Peterson, G. W.; Parsons, G. N. Catalytic “MOF-cloth” formed via directed supramolecular assembly of UiO-66-NH₂ crystals on atomic layer deposition-coated textiles for rapid degradation of chemical warfare agent simulants. *Chem. Mater.* **2017**, *29*, 4894–4903.
6. Kirlikovali, K. O.; Chen, Z.; Islamoglu, T.; Hupp, J. T.; Farha, O. K. Zirconium-based metal-organic frameworks for the catalytic hydrolysis of organophosphorus nerve agents. *ACS Appl. Mater. Interfaces* **2020**, *12*, 14702-14720.
7. Islamoglu, T.; Atilgan, A.; Moon, S. Y.; Peterson, G. W.; DeCoste, J. B.; Hall, M.; Hupp, J. T.; Farha, O. K. Cerium(IV) vs zirconium(IV) based metal-organic frameworks for detoxification of a nerve agent. *Chem. Mater.* **2017**, *29*, 2672–2675.
8. Moon, S. Y.; Prousaloglou, E.; Peterson, G. W.; DeCoste, J. B.; Hall, M. G.; Howarth, A. J.; Hupp, J. T.; Farha, O. K. Detoxification of chemical warfare agents using a Zr₆-based metal-organic framework/polymer mixture. *Chem. Eur. J.* **2016**, *22*, 14864–14868.
9. Wei, Y.-S.; Sun, L.; Wang, M.; Hong, J.; Zou, L.; Liu, H.; Wang, Y.; Zhang, M.; Liu, Z.; Li, Y.; et al. Fabricating Dual-Atom Iron Catalysts for Efficient Oxygen

Evolution Reaction: A Heteroatom Modulator Approach, *Angew. Chem. Int. Ed.* **2020**, *59*, 16013-16022.

10. Li, P.; Moon, S. Y.; Guelta, M. A.; Harvey, S. P.; Hupp, J. T.; Farha, O. K. Encapsulation of a nerve agent detoxifying enzyme by a mesoporous zirconium metal-organic framework engenders thermal and long-term stability. *J. Am. Chem. Soc.* **2016**, *138*, 8052–8055.
11. Peterson, G. W.; Moon, S. Y.; Wagner, G. W.; Hall, M. G.; DeCoste, J. B.; Hupp, J. T.; Farha, O. K. Tailoring the pore size and functionality of UiO-type metal-organic frameworks for optimal nerve agent destruction. *Inorg. Chem.* **2015**, *54*, 9684–9686.
12. Abazari, R.; Esrafil, L.; Morsali, A.; Wu, Y.; Gao, J. $\text{PMo}_{12}@$ UiO-67 nanocomposite as a novel non-leaching catalyst with enhanced performance durability for sulfur removal from liquid fuels with exceptionally diluted oxidant. *Appl. Catal. B* **2021**, *283*, 119582.
13. Liu, Y.; Moon, S. Y.; Hupp, J. T.; Farha, O. K. Dual-function metal-organic frameworks as a versatile catalyst for detoxifying chemical warfare agent simulants. *ACS Nano* **2015**, *9*, 12358–12364.

14. Li, P.; Klet, R. C.; Moon, S. Y.; Wang, T. C.; Deria, P. A.; Peters, W.; Klahr, B. M.; Park, H.; Al-Juaid, S. S.; Hupp, J. T.; et al. Synthesis of nanocrystals of Zr-based metal-organic frameworks with csq-net: significant enhancement in the degradation of a nerve agent simulant. *Chem. Commun.* **2015**, *51*, 10925–10928.
15. Moon, S. Y.; Wagner, G. W.; Mondloch, J. E.; Peterson, G. W.; DeCoste, J. B.; Hupp, J. T.; Farha, O. K. Effective, facile, and selective hydrolysis of the chemical warfare agent VX using Zr₆-based metal-organic frameworks. *Inorg. Chem.* **2015**, *54*, 10829–10833.
16. Katz, M. J.; Klet, R. C.; Moon, S. Y.; Mondloch, J. E.; Hupp, J. T.; Farha, O. K. One step backward is two steps forward: enhancing the hydrolysis rate of UiO-66 by decreasing [OH⁻]. *ACS Catal.* **2015**, *5*, 4637–4642.
17. Tabe, H.; Matushima, M.; Tanaka, R.; Yamada, Y. Creation and stabilisation of tuneable open metal sites in thiocyanato-bridged heterometallic coordination polymers to be used as heterogeneous catalysts. *Dalton Trans.* **2019**, *48*, 17063-17069.

18. Kirchon, A.; Feng, L.; Drake, H, F.; Joseph, E, A.; Zhou, H, C. From fundamentals to applications: a toolbox for robust and multifunctional MOF materials. *Chem. Soc. Rev.* **2018**, *47*, 8611-8638.
19. Ding, M.; Cai, X.; Jiang, H, L. Improving MOF stability: approaches and applications. *Chem. Sci.* **2019**, *10*, 10209-10230.
20. Nunes, P.; Gomes, A. C.; Pillinger, M.; Goncalves, I. S.; Abrantes, M. Promotion of phosphoester hydrolysis by the Zr^{IV}-based metal-organic framework UiO-67. *Microporous Mesoporous Mater.* **2015**, *208*, 21-29.
21. Witzel, M.; Ziegler, B.; Babel, D. Die kristallstruktur der hydratisierten cyanokomplex NMe₄Mn^{III}[(Mn, Cr)^{III}(CN)₆] 3H₂O und NMe₄Cd[M^{III}(CN)₆] 3H₂O (M^{III}-Fe, Co): verwandte des berliner blaus. *Anorg. Allg. Chem.* **2000**, *626*, 471–477.
22. Bal, B.; Ganguli, S.; Bhattacharya, M. Bonding of water molecules in Prussian blue: a differential thermal analysis and nuclear magnetic resonance study. *J. Phys. Chem.* **1984**, *88*, 4575–4577.
23. Rodríguez-García, B.; Reyes-Carmona, A.; Jimenez-Morales, I.; Cavaliere, S.; Blasco-Ahicart, M.; Dupont, M.; Jones, D.; Roziere, J.; Galán-Mascarós, J. R.; Jaouen, F. Cobalt hexacyanoferrate supported on Sb-doped SnO₂ as a non-noble

- catalyst for oxygen evolution in acidic medium. *Sustain. Energy Fuels* **2018**, *2*, 589–597.
24. Vazquez-Gonzalez, M.; Torrente-Rodríguez, R. M.; Kozell, A.; Liao, W. C.; Ceconello, A.; Campuzano, S.; Pingarron, J. M.; Willner, I. Mimicking peroxidase activities with Prussian blue nanoparticles and their cyanometalate structural analogues. *Nano Lett.* **2017**, *17*, 4958–4963.
25. Ghobadi, T. G. U.; Ozbay, E.; Karadas, F. How to Build Prussian Blue Based Water Oxidation Catalytic Assemblies: Common Trends and Strategies. *Chem.–Eur. J.* **2020**, *27*, 3638–3649.
26. Lin, K. Y. A.; Chen, B. J.; Chen, C. K. Evaluating Prussian blue analogues $M^{II}_3[M^{III}(CN)_6]_2$ ($M^{II} = Co, Cu, Fe, Mn, Ni$; $M^{III} = Co, Fe$) as activators for peroxymonosulfate in water. *RSC Adv.* **2016**, *6*, 92923–92933.
27. Han, L. J.; Tang, P.; Reyes-Carmona, A.; Rodríguez-García, B.; Torrens, M.; Morante, J. R.; Arbiol, J.; Galán-Mascarós, J. R. Enhanced activity and acid pH stability of Prussian blue-type oxygen evolution electrocatalysts processed by chemical etching. *J. Am. Chem. Soc.* **2016**, *138*, 16037–16045.

28. Goberna-Ferron, S.; Hernandez, W. Y.; Rodríguez-García, B.; Galán-Mascarós, J. R. Light-driven water oxidation with metal hexacyanometallate heterogeneous catalysts. *ACS Catal.* **2014**, *4*, 1637–1641.
29. Pintado, S.; Goberna-Ferrón, S.; Escudero-Adan, E. C.; Galán-Mascarós, R. J.; Fast and persistent electrocatalytic water oxidation by Co-Fe Prussian blue coordination polymers. *J. Am. Chem. Soc.* **2013**, *135*, 13270–13273.
30. Aratani, Y.; Suenobu, T.; Ohkubo, K.; Yamada, Y.; Fukuzumi, S. Dual function photocatalysis of cyano-bridged heteronuclear metal complexes for water oxidation and two-electron reduction of dioxygen to produce hydrogen peroxide as a solar fuel. *Chem. Commun.* **2017**, *53*, 3473–3476.
31. Yamada, Y.; Oyama, K.; Suenobu, T.; Fukuzumi, S. Photocatalytic water oxidation by persulphate with a Ca²⁺ ion-incorporated polymeric cobalt cyanide complex affording O₂ with 200% quantum efficiency. *Chem. Commun.* **2017**, *53*, 3418–3421.
32. Isaka, Y.; Oyama, K.; Yamada, Y.; Suenobu, T.; Fukuzumi, S. Production of hydrogen peroxide by combination of semiconductor-photocatalysed oxidation of water and photocatalytic two-electron reduction of dioxygen. *Catal. Sci. Technol.* **2016**, *6*, 681–684.

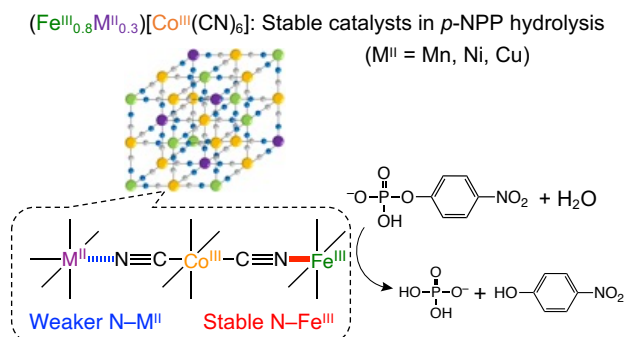
33. Yamada, Y.; Oyama, K.; Gates, R.; Fukuzumi, S. High catalytic activity of heteropolynuclear cyanide complexes containing cobalt and platinum ions: visible-light driven water oxidation. *Angew. Chem. Int. Ed.* **2015**, *54*, 5613–5617.
34. Yamada, Y.; Yoneda, M.; Fukuzumi, S. High power density of one-compartment H₂O₂ fuel cells using pyrazine-bridged Fe[M^C(CN)₄] (M^C = Pt²⁺ and Pd²⁺) complexes as the cathode. *Inorg. Chem.* **2014**, *53*, 1272–1274.
35. Yamada, Y.; Yoneda, M.; Fukuzumi, S. A robust one-compartment fuel cell with a polynuclear cyanide complex as a cathode for utilizing H₂O₂ as a sustainable fuel at ambient conditions. *Chem. –Eur. J.* **2013**, *19*, 11733–11741.
36. Tabe, H.; Kitase, A.; Yamada, Y. Utilization of core-shell nanoparticles to evaluate subsurface contribution to water oxidation catalysis of [Co^{II}(H₂O)₂]_{1.5}[Co^{III}(CN)₆] nanoparticles. *Appl. Catal. B* **2020**, *262*, 118101.
37. Yamane, M.; Tabe, H.; Kawakami, M.; Tanaka, H.; Kawamoto, T.; Yamada, Y. Single open sites on Fe^{II} ions stabilized by coupled metal ions in CN-deficient Prussian blue analogues for high catalytic activity in the hydrolysis of organophosphates. *Inorg. Chem.* **2020**, *59*, 16000–16009.

38. Tabe, H.; Terashima, C.; Yamada, Y. Effect of surface acidity of cyano-bridged polynuclear metal complexes on the catalytic activity for the hydrolysis of organophosphates. *Catal. Sci. Technol.* **2018**, *8*, 4747–4756.
39. Alozi, M.; Rawas-Qalaji, M., Treating organophosphates poisoning: management challenges and potential solutions. *Crit. Rev. Toxicol* **2020**, *50*, 764-779.
40. Parween, T.; Jan, S., Ecophysiology of Pesticides: Interface between pesticide chemistry and plant physiology. 1st Edition ed.; *Academic Press: Massachusetts*, **2019**; Vol. 12.
41. Costa, L. Organophosphorus compounds at 80: some old and new issues. *Toxicol. Sci.* **2018**, *162*, 24–35.
42. Munoz-Quezada, M. T.; Lucero, B. A.; Barr, D. B.; Steenland, K.; Levy, K.; Ryan, P. B.; Iglesias, V.; Alvarado, S.; Concha, C.; Rojas, E.; et al. Neurodevelopmental effects in children associated with exposure to organophosphate pesticides: a systematic review. *Neurotoxicology* **2013**, *39*, 158–168.
43. Sharma, N.; Kakkar, R. Recent advancements on warfare agents/metal oxides surface chemistry and their simulation study. *Adv. Mater. Lett.* **2013**, *4*, 508–521.

44. Smith, B. M. Catalytic methods for the destruction of chemical warfare agents under ambient conditions. *Chem. Soc. Rev.* **2008**, *37*, 470–478.
45. Moon, S. Y.; Liu, Y.; Hupp, J. T.; Farha, O. K. Instantaneous hydrolysis of nerve-agent simulants with a six-connected zirconium-based metal-organic framework. *Angew. Chem. Int. Ed.* **2015**, *54*, 6795–6799.
46. Mondloch, J. E.; Katz, M. J.; Isley, W. C.; Ghosh, P.; Liao, P.; Bury, W.; Wagner, G. W.; Hall, M. G.; DeCoste, J. B.; Peterson, G. W.; et al. Destruction of chemical warfare agents using metal-organic frameworks. *Nat. Mater.* **2015**, *14*, 512–516.
47. Katz, M. J.; Mondloch, J. E.; Totten, R. K.; Park, J. K.; Nguyen, S. T.; Farha, O. K.; Hupp, J. T. Simple and compelling biomimetic metal-organic frameworks catalyst for the degradation of nerve agent simulants. *Angew. Chem. Int. Ed.* **2014**, *53*, 497–501.
48. Catafesta, J.; Haines, J.; Zorzi, J. E.; Pereira, A. S.; Perottoni, C. A. Pressure-induced amorphization and decomposition of Fe[Co(CN)₆]. *Phys. Rev. B* **2008**, *77*, 064104.
49. Nakamoto, K. *Infrared and Raman Spectra of Inorganic and Coordination Compounds*, 4th ed.; Wiley Interscience: New York, 1986.

50. Simonov, A.; De Baerdemaeker, T.; Boström, H. L. B.; Gómez, M. L. R.; Gray, H. J.; Chernyshov, D.; Bosak, A.; Bürgi, H. B.; Goodwin, A. L. Hidden diversity of vacancy networks in Prussian blue analogues. *Nature* **2020**, *578*, 256-260.
51. Wang, Z.; Huang, Y.; Luo, R.; Wu, F.; Li, L.; Xie, M.; Huang, J., Chen, R. Ion-exchange synthesis of high-energy-density prussian blue analogues for sodium ion battery cathodes with fast kinetics and long durability. *J. Power Sources* **2019**, *436*, 226868.
52. Iveković, D.; Trbić, H. V.; Peter, R.; Petravić, M.; Čeh, M.; Pihlar, B. Enhancement of stability of Prussian blue thin films by electrochemical insertion of Ni²⁺ ions: A stable electrocatalytic sensing of H₂O₂ in mild alkaline media. *Electrochim. Acta* **2012**, *78*, 452-458.
53. Ishizaki, M.; Ohshida, E.; Tanno, H.; Kawamoto, T.; Tanaka, H.; Hara, K.; Kominami, H.; Kurihara, M. H₂O₂-sensing abilities of mixed-metal (Fe-Ni) Prussian blue analogs in a wide pH range. *Inorg. Chim. Acta* **2020**, *502*, 119314-119319.

TOC Graphic



Synopsis

Catalytic stability of cyano-bridged polynuclear complexes were dramatically enhanced by doping M^{II} ions for the catalytic *p*-nitrophenyl phosphate hydrolysis in aqueous media.

The mechanism of catalytic stability enhancement was scrutinized by IR and surface acidity measurements. Doping of M^{II} ions results in secure $\text{Fe}^{\text{III}}\text{-N}$ bonds to avoid leaching of Fe ions from the framework.

Supporting Information
for
Mechanism for Catalytic Stability Enhancement of Fe^{III}[Co^{III}(CN)₆] by
Doping Divalent Ions for Organophosphate Hydrolysis

Yusuke Seki[†], Hiroyasu Tabe[§], and Yusuke Yamada^{*,†,‡}

[†]Department of Applied Chemistry and Bioengineering, Graduate School of Engineering, Osaka City University, 3-3-138 Sugimoto, Sumiyoshi, Osaka 558-8585, Japan

[§]Institute for Integrated Cell-Material Sciences, Institute for Advanced Study, Kyoto University, Yoshida-Hommachi, Sakyo, Kyoto 606-8501, Japan

[‡]Research Center for Artificial Photosynthesis (ReCAP), Osaka City University, 3-3-138 Sugimoto, Sumiyoshi, Osaka 558-8585, Japan

*E-mail: ymd@osaka-cu.ac.jp.

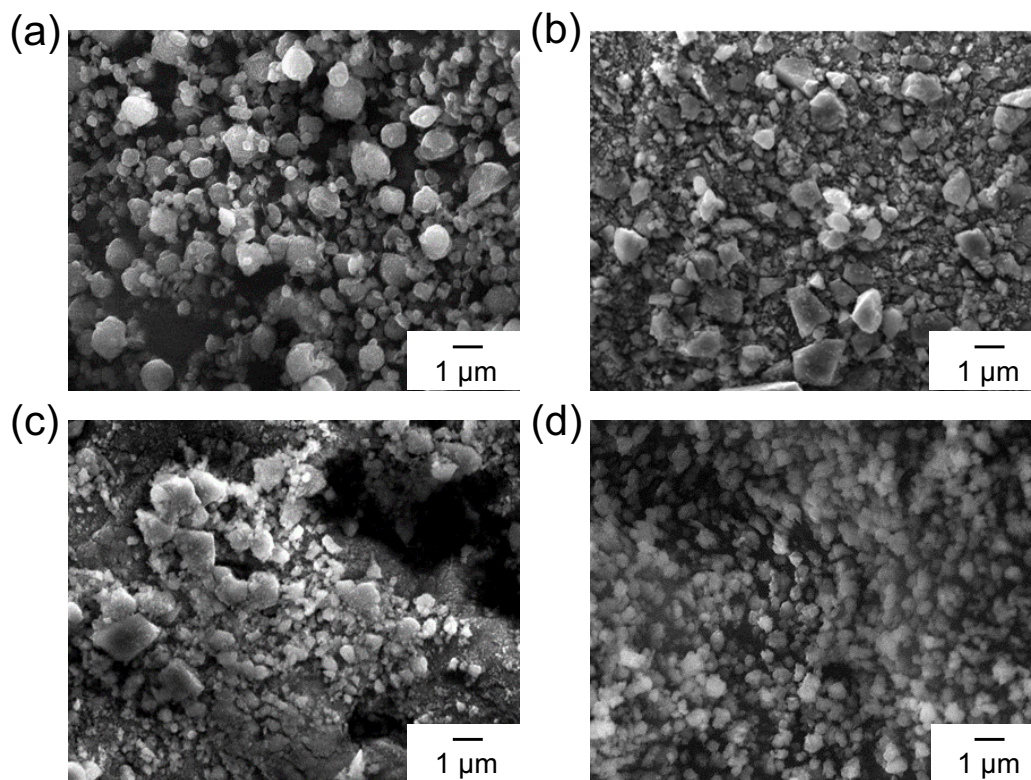


Figure S1. Scanning electron microscope (SEM) images of (a) $(\text{Fe}^{\text{III}}_{0.8}\text{Mn}^{\text{II}}_{0.3})[\text{Co}^{\text{III}}(\text{CN})_6]$ (**FeMn-Co**), (b) $(\text{Fe}^{\text{III}}_{0.8}\text{Ni}^{\text{II}}_{0.3})[\text{Co}^{\text{III}}(\text{CN})_6]$ (**FeNi-Co**), (c) $(\text{Fe}^{\text{III}}_{0.8}\text{Cu}^{\text{II}}_{0.3})[\text{Co}^{\text{III}}(\text{CN})_6]$ (**FeCu-Co**), and (d) $\text{Fe}^{\text{III}}[\text{Co}^{\text{III}}(\text{CN})_6]$ (**Fe-Co**).

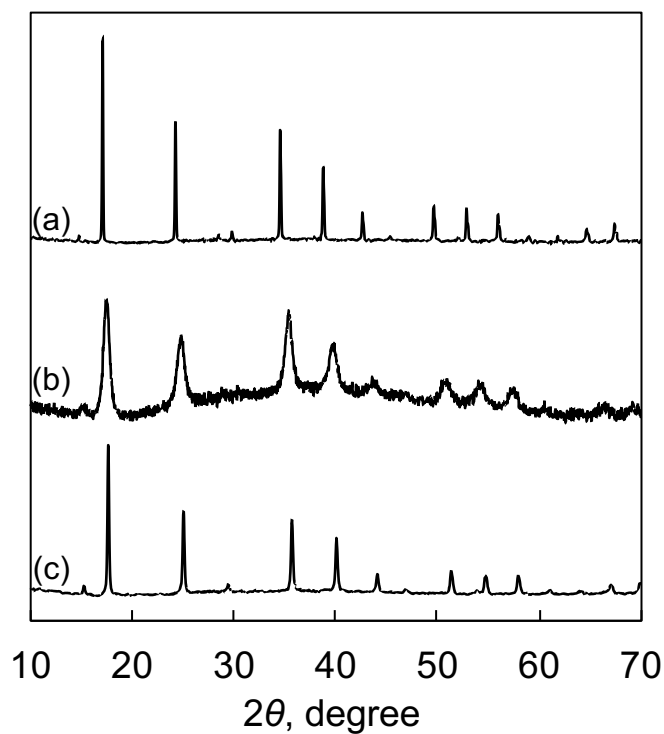


Figure S2. Powder X-ray diffraction (PXRD) patterns of (a) $\text{Mn}^{\text{II}}_{1.5}[\text{Co}^{\text{III}}(\text{CN})_6]$ (**Mn-Co**), (b) $\text{Ni}^{\text{II}}_{1.5}[\text{Co}^{\text{III}}(\text{CN})_6]$ (**Ni-Co**), and (c) $\text{Cu}^{\text{II}}_{1.5}[\text{Co}^{\text{III}}(\text{CN})_6]$ (**Cu-Co**).

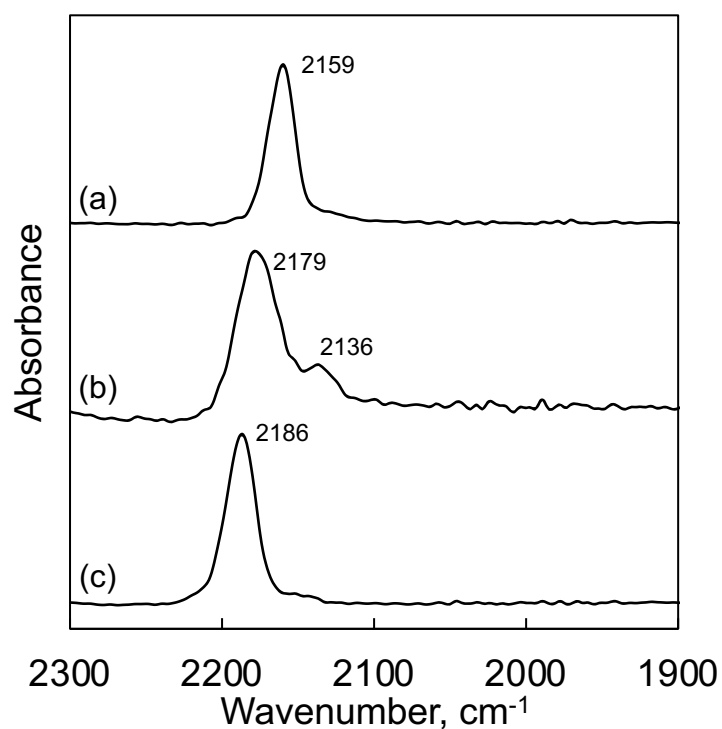


Figure S3. Infrared spectra of (a) $\text{Mn}^{\text{II}}_{1.5}[\text{Co}^{\text{III}}(\text{CN})_6]$ (**Mn-Co**), (b) $\text{Ni}^{\text{II}}_{1.5}[\text{Co}^{\text{III}}(\text{CN})_6]$ (**Ni-Co**), and (c) $\text{Cu}^{\text{II}}_{1.5}[\text{Co}^{\text{III}}(\text{CN})_6]$ (**Cu-Co**).

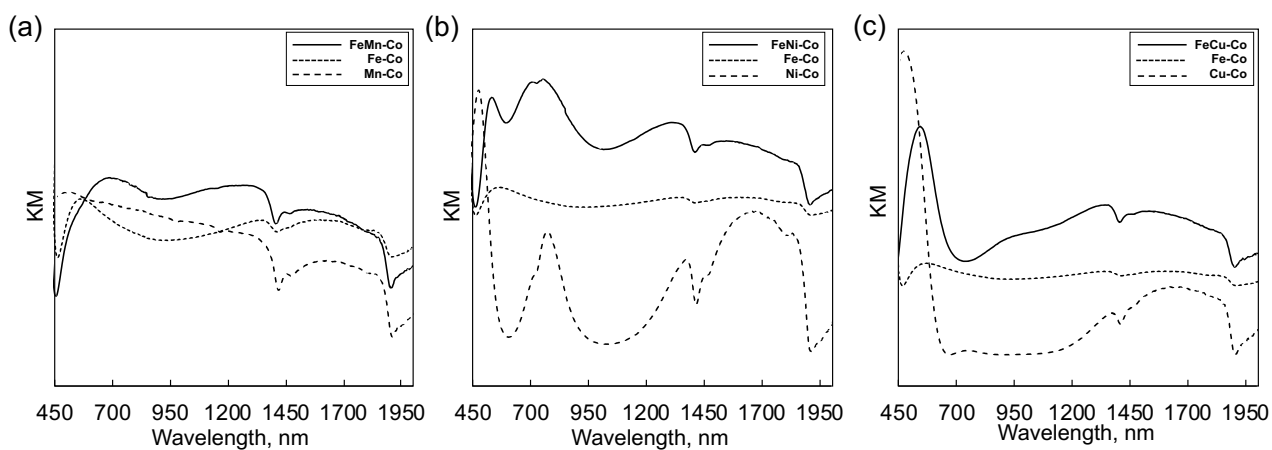


Figure S4. UV-vis-near IR reflectance spectra of (a) $(\text{Fe}^{\text{III}}_{0.8}\text{Mn}^{\text{II}}_{0.3})[\text{Co}^{\text{III}}(\text{CN})_6]$ (**FeMn-Co**), (b) $(\text{Fe}^{\text{III}}_{0.8}\text{Ni}^{\text{II}}_{0.3})[\text{Co}^{\text{III}}(\text{CN})_6]$ (**FeNi-Co**), and (c) $(\text{Fe}^{\text{III}}_{0.8}\text{Cu}^{\text{II}}_{0.3})[\text{Co}^{\text{III}}(\text{CN})_6]$.

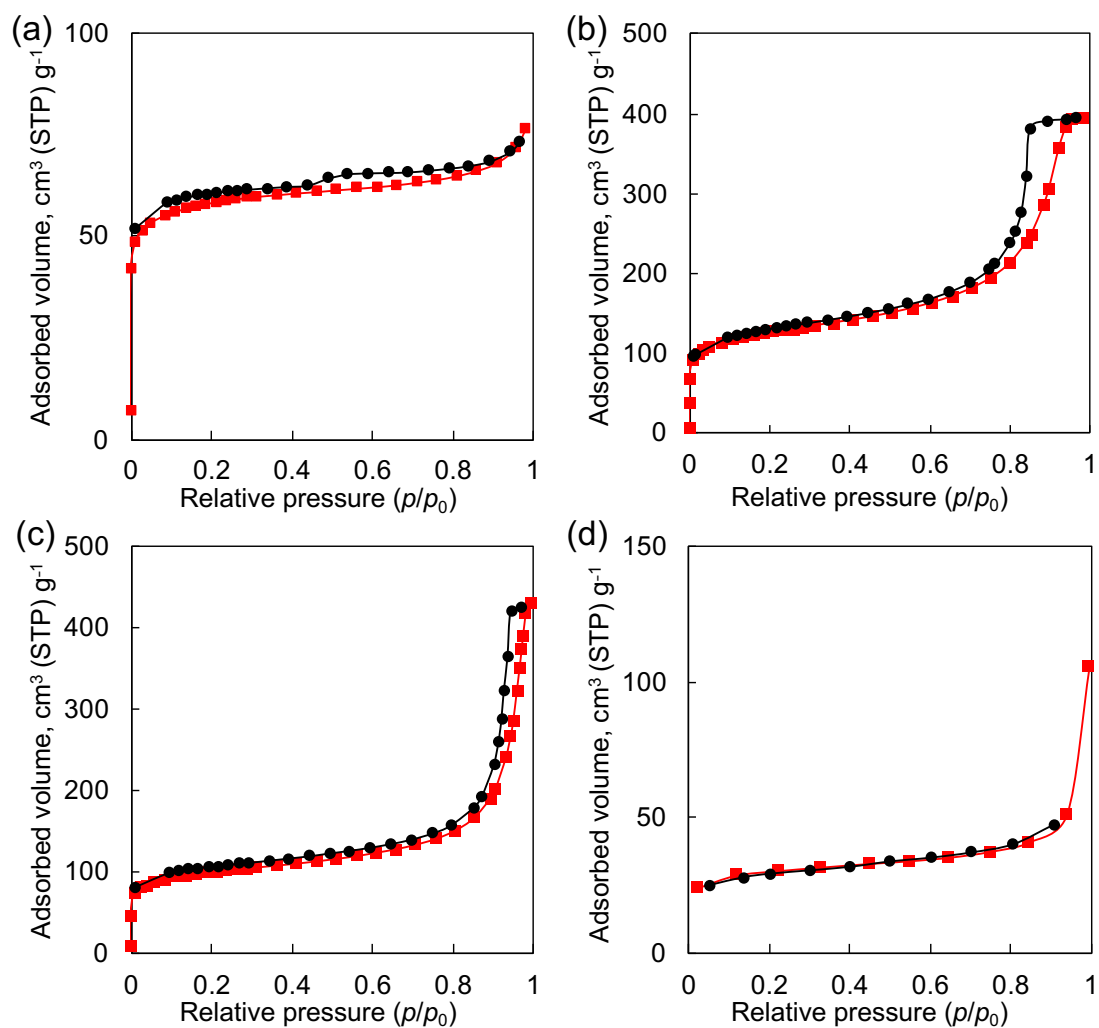


Figure S5. Nitrogen adsorption (red squares)-desorption (black circles) of (a) $(\text{Fe}^{\text{III}}_{0.8}\text{Mn}^{\text{II}}_{0.3})[\text{Co}^{\text{III}}(\text{CN})_6]$ (**FeMn-Co**), (b) $(\text{Fe}^{\text{III}}_{0.8}\text{Ni}^{\text{II}}_{0.3})[\text{Co}^{\text{III}}(\text{CN})_6]$ (**FeNi-Co**), (c) $(\text{Fe}^{\text{III}}_{0.8}\text{Cu}^{\text{II}}_{0.3})[\text{Co}^{\text{III}}(\text{CN})_6]$ (**FeCu-Co**), and (d) $\text{Fe}^{\text{III}}[\text{Co}^{\text{III}}(\text{CN})_6]$ (**Fe-Co**).

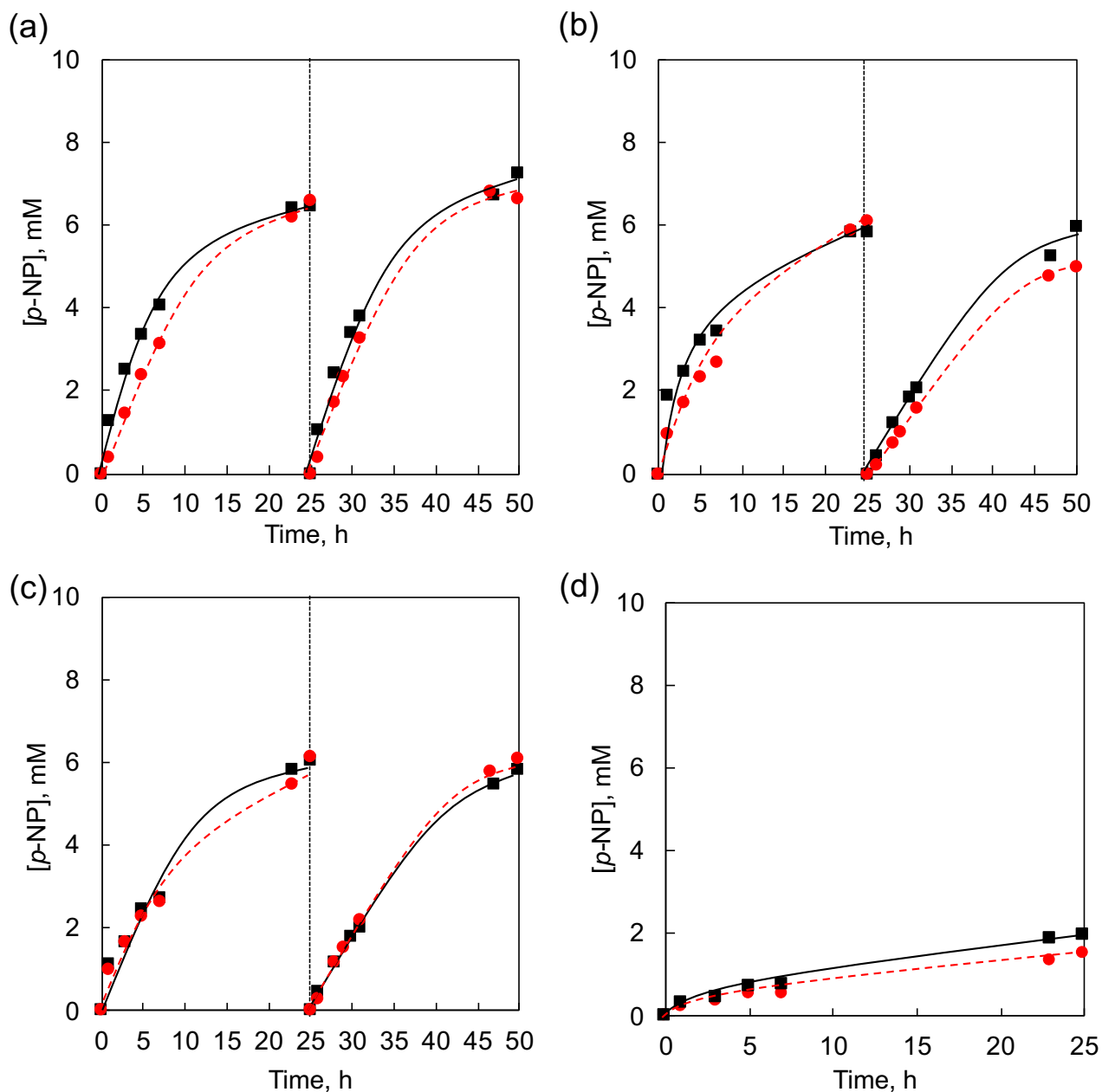


Figure S6. (Reproducibility check) Time course of the formation of *p*-nitrophenol (*p*-NP) in a mixed solution of water and ethanol [9:1 (v/v), 0.75 mL] containing disodium *p*-nitrophenyl phosphate (*p*-NPP, 10 mM) and $(\text{Fe}^{\text{III}}_{0.8}\text{M}^{\text{II}}_{0.3})[\text{Co}^{\text{III}}(\text{CN})_6]$ (3.0 mg) [$\text{M} =$ (a) Mn^{II} , (b) Ni^{II} , and (c) Cu^{II}] or (d) $\text{Fe}^{\text{III}}[\text{Co}^{\text{III}}(\text{CN})_6]$ for 1st replicates (black solid line, ■) and 2nd replicates (red dotted line, ●).

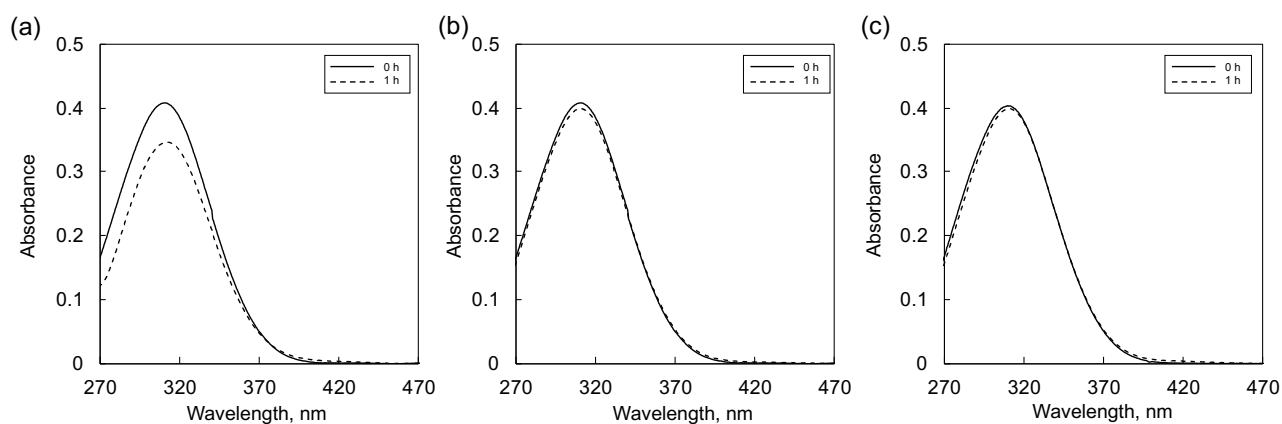


Figure S7. UV-visible spectra of a mixed solution of water and ethanol [9:1 (v/v), 0.75 mL] containing disodium *p*-nitrophenyl phosphate (*p*-NPP, 10 mM) and $M^{II}_{1.5}[Co^{III}(CN)_6]$ (3.0 mg) [$M =$ (a) Mn^{II} , (b) Ni^{II} , and (c) Cu^{II}]. The spectra were obtained by adding an aliquot (10 μ L) of the reaction solution in a HEPES-NaOH buffer solution (2490 μ L, 0.1 M, pH 8.3). The peaks at 310 and 400 nm are assignable *p*-nitrophenyl phosphate (*p*-NPP) and *p*-nitrophenolate ion (*p*-NP), respectively.

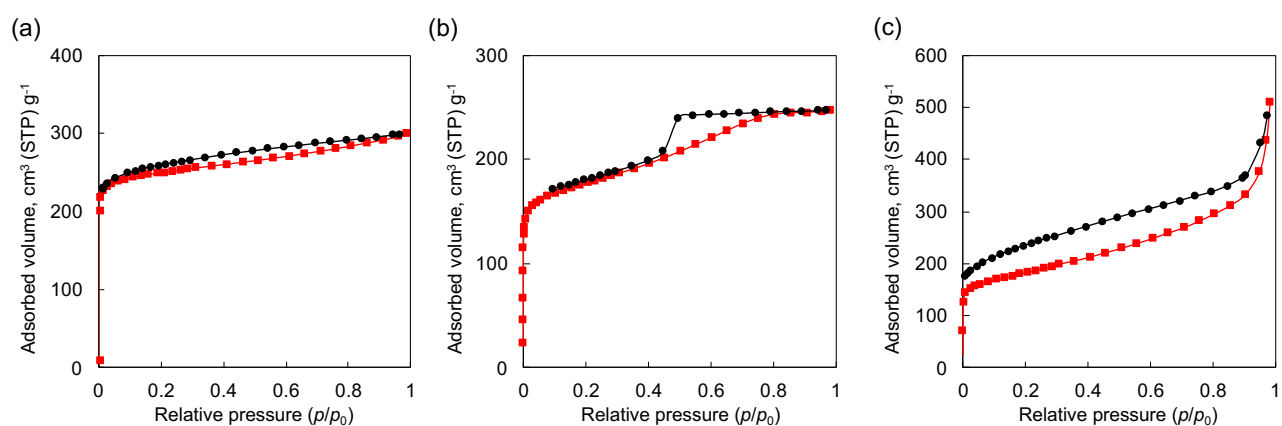


Figure S8. Nitrogen adsorption (red squares, ■)-desorption (black circles, ●) of (a) $Mn^{II}_{1.5}[Co^{III}(CN)_6]$ (**Mn-Co**), (b) $Ni^{II}_{1.5}[Co^{III}(CN)_6]$ (**Ni-Co**), and (c) $Cu^{II}_{1.5}[Co^{III}(CN)_6]$ (**Cu-Co**).

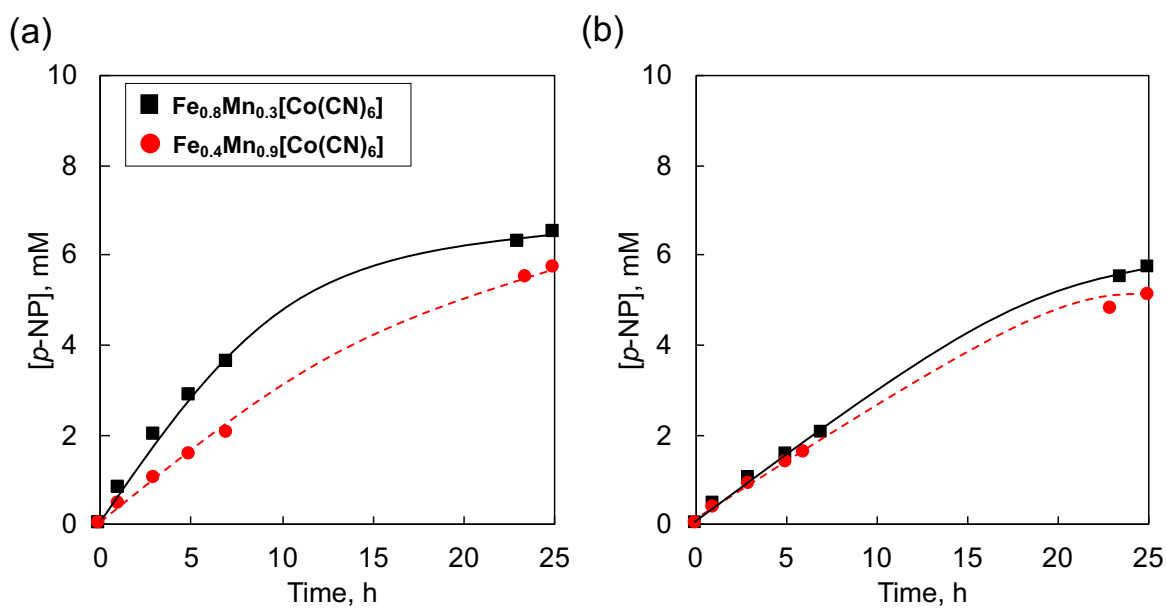


Figure S9. (a) Time course of the formation of *p*-nitrophenol (*p*-NP) in a mixed solution of water and ethanol [9:1 (v/v), 0.75 mL] containing disodium *p*-nitrophenyl phosphate (*p*-NPP, 10 mM) and $(\text{Fe}^{\text{III}}_{0.8}\text{Mn}^{\text{II}}_{0.3})[\text{Co}^{\text{III}}(\text{CN})_6]$ (■, 3.0 mg) or $(\text{Fe}^{\text{III}}_{0.4}\text{Mn}^{\text{II}}_{0.9})[\text{Co}^{\text{III}}(\text{CN})_6]$ (●). (b) Time course of the formation of *p*-nitrophenol (*p*-NP) in a mixed solution of water and ethanol [9:1 (v/v), 0.75 mL] containing disodium *p*-nitrophenyl phosphate (*p*-NPP, 10 mM) and $(\text{Fe}^{\text{III}}_{0.4}\text{Mn}^{\text{II}}_{0.9})[\text{Co}^{\text{III}}(\text{CN})_6]$ (3.0 mg) for 1st replicates (black solid line, ■) and 2nd replicates (red dashed line, ●).

Table S1. Comparison of catalytic activity and stability of cyano-bridged coordination polymers for the hydrolysis of *p*-nitrophenyl phosphate (*p*-NPP).

Cyano-Bridged Coordination Polymer	Media	[<i>p</i> -NPP]/[M ^N]	Conversion at 1 st run (%)	Conversion at 2 nd run (%)	Ref.
[Cu ^{II} (H ₂ O) _{8/3}] _{1.5} [Fe ^{II} (CN) ₅ (NH ₃)]	HEPES buffer (pH 6.0)	3.4	42 (24 h)	13 (24 h)	37
[Fe ^{III} (H ₂ O) _{1.5}] _{4/3} [Fe ^{II} (CN) ₆]	HEPES buffer (pH 8.0)	2.4	79 (8 h)	56 (8 h)	38
Fe ^{III} [Ir ^{III} (CN) ₆]	HEPES buffer (pH 8.0)	2.5	90 (25 h)	–	38
[Fe ^{III} (H ₂ O) _{1.5}] _{4/3} [Ru ^{II} (CN) ₆]	HEPES buffer (pH 8.0)	0.5	81 (60 h)	–	38
(Fe ^{III} _{0.8} Mn ^{II} _{0.3})[Co ^{III} (CN) ₆]	Water and ethanol (9/1)	1.5	65 (25 h)	69 (25 h)	This work
(Fe ^{III} _{0.8} Ni ^{II} _{0.3})[Co ^{III} (CN) ₆]	Water and ethanol (9/1)	1.5	60 (25 h)	55 (25 h)	This work
(Fe ^{III} _{0.8} Cu ^{II} _{0.3})[Co ^{III} (CN) ₆]	Water and ethanol (9/1)	1.5	61 (25 h)	60 (25 h)	This work

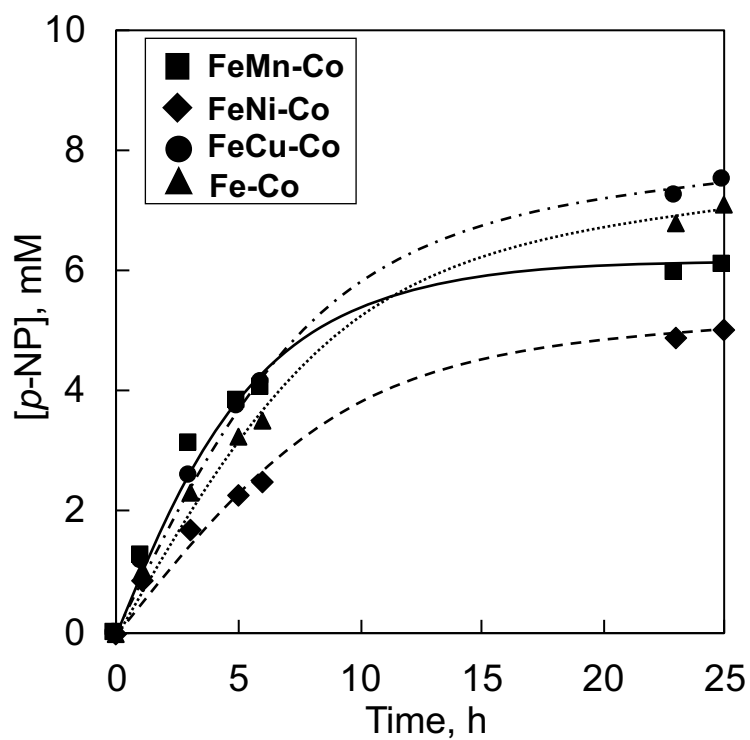


Figure S10. Time course of the formation of *p*-nitrophenol (*p*-NP) in a HEPES buffer solution (pH 8.0, 100 mM, 0.75 mL) containing disodium *p*-nitrophenyl phosphate (*p*-NPP, 10 mM) and $(\text{Fe}^{\text{III}}_{0.8}\text{Mn}^{\text{II}}_{0.3})[\text{Co}^{\text{III}}(\text{CN})_6]$ (**FeMn-Co**) (■, 3.0 mg), $(\text{Fe}^{\text{III}}_{0.8}\text{Ni}^{\text{II}}_{0.3})[\text{Co}^{\text{III}}(\text{CN})_6]$ (**FeNi-Co**) (◆), $(\text{Fe}^{\text{III}}_{0.8}\text{Cu}^{\text{II}}_{0.3})[\text{Co}^{\text{III}}(\text{CN})_6]$ (**FeCu-Co**) (●), and $\text{Fe}^{\text{III}}[\text{Co}^{\text{III}}(\text{CN})_6]$ (**Fe-Co**) (▲).

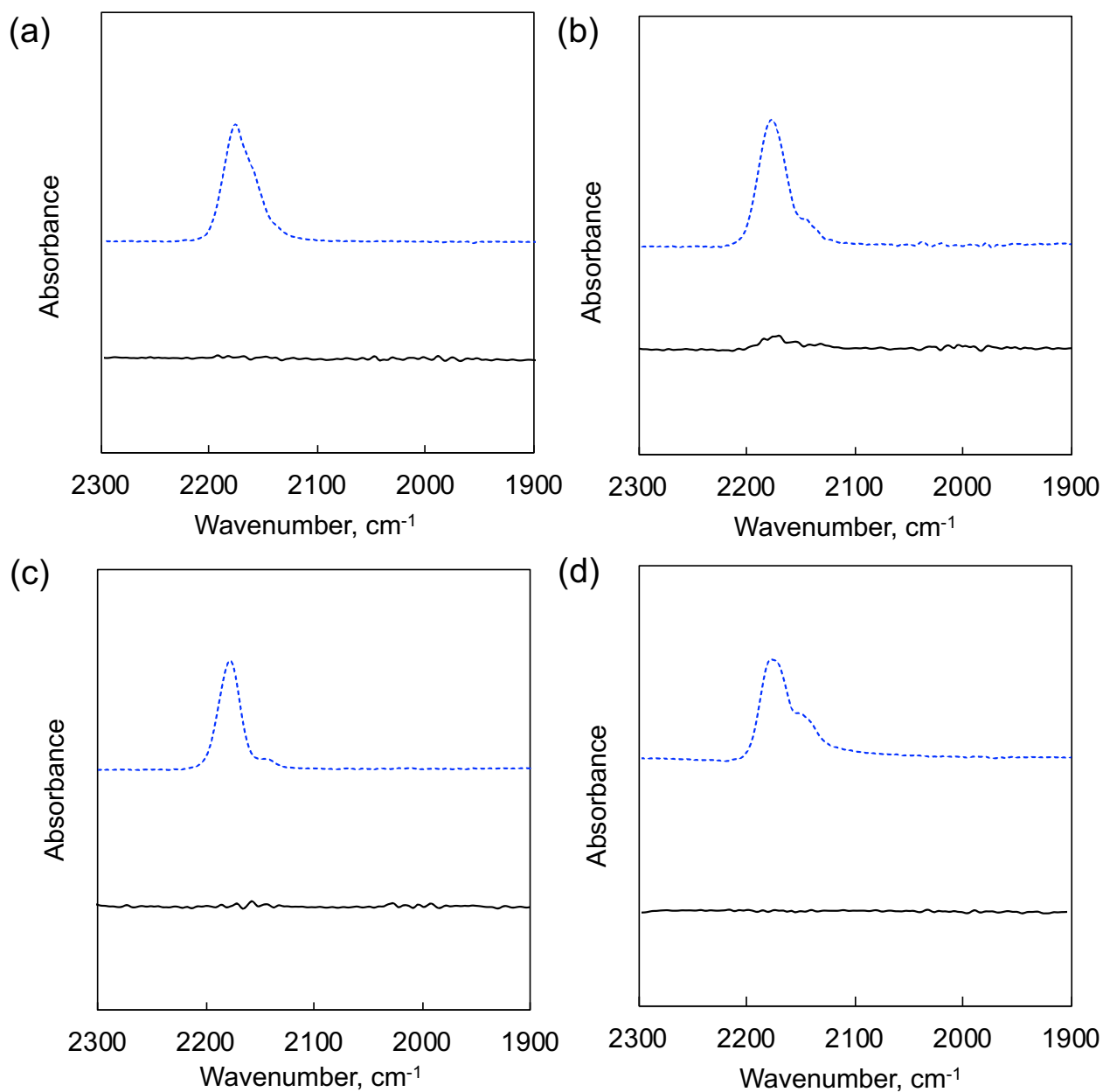


Figure S11. Infrared (IR) spectra of (a) $(\text{Fe}^{\text{III}}_{0.8}\text{Mn}^{\text{II}}_{0.3})[\text{Co}^{\text{III}}(\text{CN})_6]$ (**FeMn-Co**), (b) $(\text{Fe}^{\text{III}}_{0.8}\text{Ni}^{\text{II}}_{0.3})[\text{Co}^{\text{III}}(\text{CN})_6]$ (**FeNi-Co**), (c) $(\text{Fe}^{\text{III}}_{0.8}\text{Cu}^{\text{II}}_{0.3})[\text{Co}^{\text{III}}(\text{CN})_6]$ (**FeCu-Co**), and (d) $\text{Fe}^{\text{III}}[\text{Co}^{\text{III}}(\text{CN})_6]$ (**Fe-Co**) before (blue dotted lines) and after (black solid lines) the hydrolysis of *p*-nitrophenyl phosphate (*p*-NPP, 10 mM) in a HEPES buffer solution (pH 8.0, 100 mM, 0.75 mL).

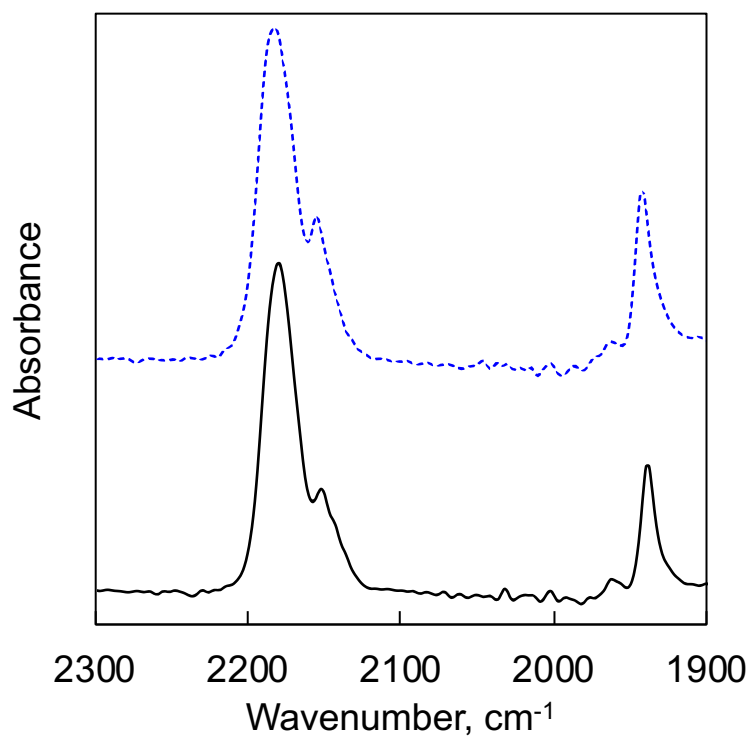


Figure S12. Infrared spectra of $\text{Fe}^{\text{III}}[\text{Co}^{\text{III}}(\text{CN})_6]$ (**Fe-Co**) before (blue dotted lines) and after (black solid lines) the catalytic reactions in the presence of internal standard (carbonylchlorohydridotris(triphenylphosphine)ruthenium(II) ($\text{Ru}^{\text{II}}(\text{CO})(\text{PPh}_3)\text{ClH}$), $\nu_{\text{CO}} = 1940 \text{ cm}^{-1}$). The catalysts were collected from a mixed solution [water and ethanol, 9:1 (v/v); 0.75 mL]. Prior to the IR measurement, the fresh and recovered catalysts (0.60 mg) were mixed with $\text{Ru}^{\text{II}}(\text{CO})(\text{PPh}_3)\text{ClH}$ (0.60 mg).

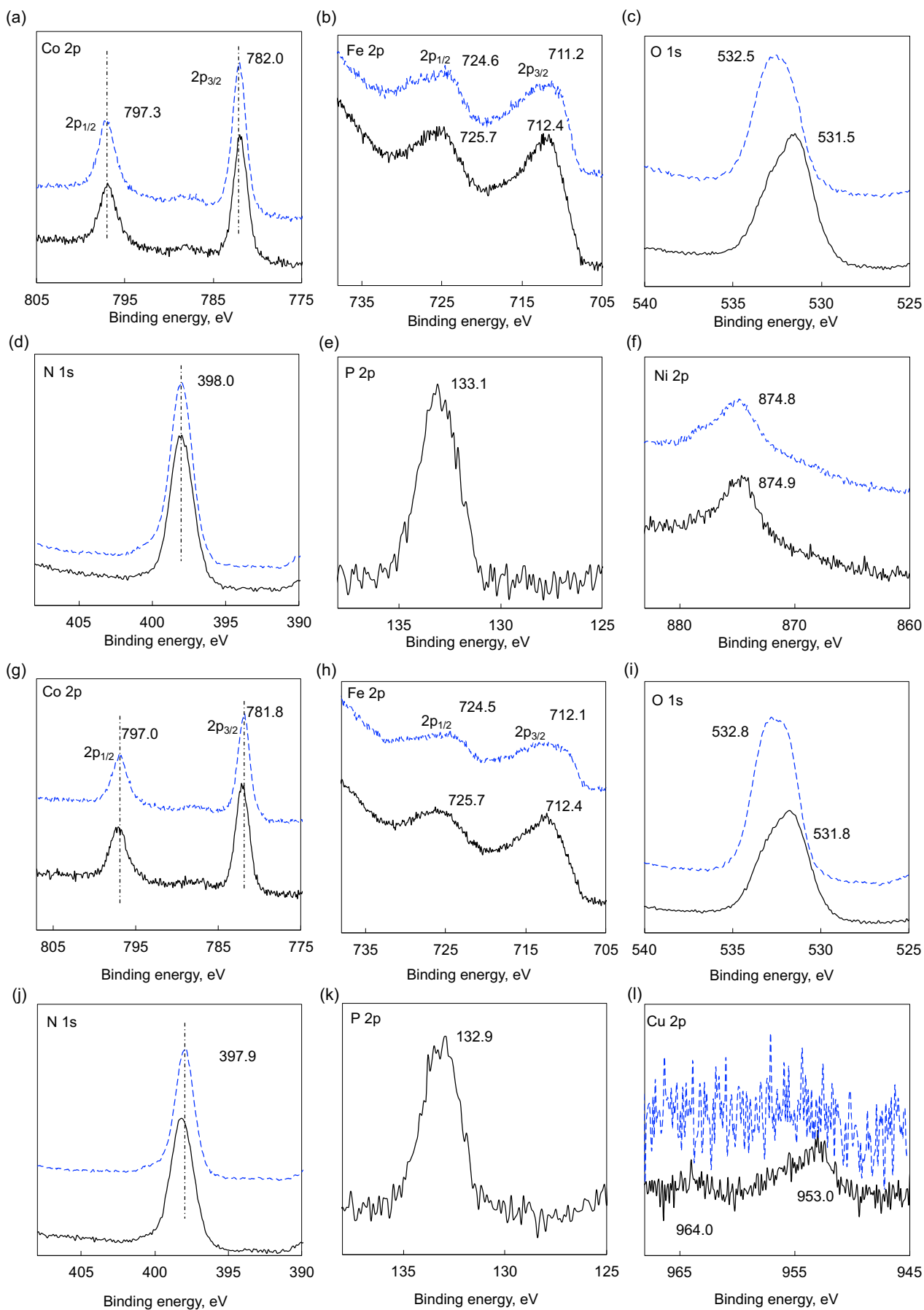


Figure S13. X-ray photoelectron spectroscopy (XPS) spectra of (a-f) $(\text{Fe}^{\text{III}}_{0.8}\text{Ni}^{\text{II}}_{0.3})[\text{Co}^{\text{III}}(\text{CN})_6]$ (**FeNi-Co**) and (g-l) $(\text{Fe}^{\text{III}}_{0.8}\text{Cu}^{\text{II}}_{0.3})[\text{Co}^{\text{III}}(\text{CN})_6]$ (**FeCu-Co**) before (blue dotted lines) and after (black solid lines) the catalytic reactions.

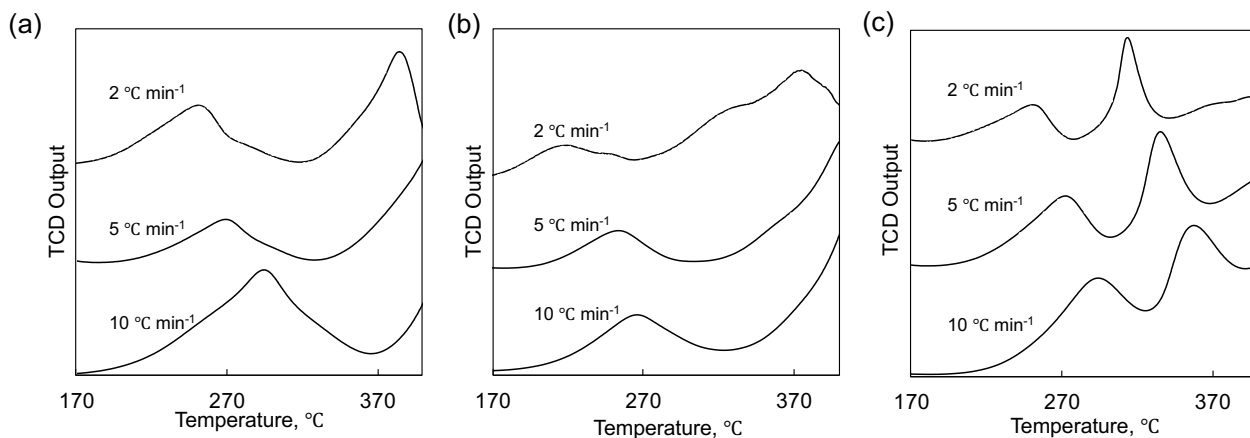


Figure S14. Temperature-programmed desorption (TPD) of pyridine spectra from (a) $(\text{Fe}^{\text{III}}_{0.8}\text{Mn}^{\text{II}}_{0.3})[\text{Co}^{\text{III}}(\text{CN})_6]$ (**FeMn-Co**), (b) $(\text{Fe}^{\text{III}}_{0.8}\text{Ni}^{\text{II}}_{0.3})[\text{Co}^{\text{III}}(\text{CN})_6]$ (**FeNi-Co**), and (c) $(\text{Fe}^{\text{III}}_{0.8}\text{Cu}^{\text{II}}_{0.3})[\text{Co}^{\text{III}}(\text{CN})_6]$ (**FeCu-Co**). TPD measurements were performed by heating with various ramp rates ranging from 2 to 10 $^{\circ}\text{C min}^{-1}$ after pretreatment (150 $^{\circ}\text{C}$ for 1 h), adsorption of pyridine (5 kPa, 100 $^{\circ}\text{C}$ for 30 min), and removal of excess pyridine (150 $^{\circ}\text{C}$ for 30 min) with a flow of helium (30 mL min^{-1}).